Study of Thermal Diffusivity of Dielectric-Metal Sandwich Structures at Low Temperatures

- Masterarbeit -

zur Erlangung des akademischen Grades
Master of Science

seit 1558

Friedrich-Schiller-Universität Jena
Institut für Festkörperphysik

eingereicht von Jessica Golm
geb. am 18.02.1986

1. Gutachter:
   Prof. Dr. P. Seidel
   Institut für Festkörperphysik
   Friedrich-Schiller-Universität Jena

2. Gutachter:
   Dr. rer. nat. T. Köttig
   CERN

Tag der Abgabe:

Contents

1. Introduction

Particle accelerators are nowadays large scale installations with the goal to answer the question: What is the universe made of? And how do these particles interact? Therefore, complex facilities are built all over the world.
One question, that has not been answered yet, is the gravitational interaction between matter and antimatter. One would expect the same behavior like between matter and matter, but there are theories, that allow different solutions for antimatter.
To answer this important question the Antihydrogen Experiment: Gravity, Interferometry, Spectroscopy (AEgIS) has been built at CERN, the European Organization for Nuclear Research (Conseil Européen pour la Recherche Nucléaire). The experiment is stationed at CERN in the Antimatter Factory and it aims to measure the earth's gravitational acceleration on antihydrogen with a precision of 1 %. Therefore an temperature of about 100 mK is required to reduce the random thermal movement of the particles [1]. It is the task of the CERN Cryolab to ensure a proper heat transport in the milliKelvin temperature range of the planned upgrade of the AEgIS ultra-low temperature region.

1.1. Antihydrogen Experiment: Gravity, Interferometry, Spectroscopy (AEgIS)

The measurement of the gravitational acceleration on antimatter with high precision as planned for AEgIS requires a neutral antiatom. Former experiments with the same goal showed a stronger influence of the Coulomb force compared to the gravitational force on an antiproton [2]. The electrical stray fields make a gravitational measurement on charged particles challenging. That is the reason why antihydrogen was chosen for these studies. To produce antihydrogen ($\bar{H}$) a beam of excited positronium (Ps^*) is shot on a cloud out of antiprotons ($\bar{p}$). These constituents recombine, the reaction equation being:

$$\bar{p} + Ps^* \rightarrow \bar{H} + e^- \quad . \tag{1}$$

For the production of antiprotons, energies higher than 5.63 GeV are required [3]. To achieve such high energies an accelerator structure like at CERN is necessary. The whole CERN accelerator complex and the particles the different accelerators are operated with is illustrated in Figure 1.1.
For the antiproton production, protons are accelerated first in a linear accelerator (LINAC 2) up to 50 MeV, afterwards the particles enter a ring accelerator with 157 m circumference (BOOSTER cf. Figure 1.1) and gain energy to 1.4 GeV. The final step, before the production of antiprotons, is a ring accelerator with a circumference of 628 m, the Proton

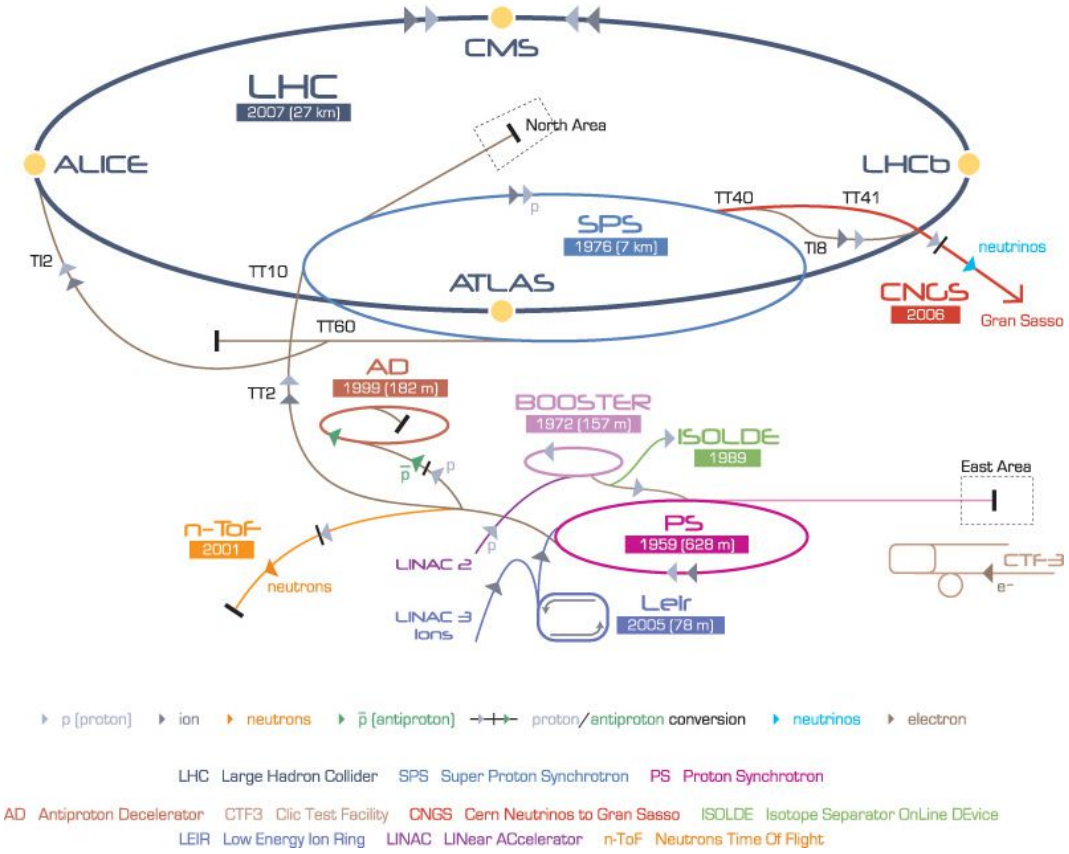

Figure 1.1: Schematics of the CERN accelerator complex [4].

Synchrotron (PS), which can accelerate the particles up to 25 GeV. At these energies the protons are guided on a target. By hitting the nucleus with a proton an antiproton pair is created. These antiprotons have high energies - much too high to investigate their properties or to use them for recombination with other particles. This is why the created anti-particles are slowed down in the Antiproton Decelerator (AD cf. Figure 1.1). The structure reduces the energy of the antiprotons down to 5.3 MeV [5]. The antiprotons can now be accumulated and slowed down further for recombination in each of the experiments.

To accumulate charged particles Penning traps are used, which use a magnetic field to force the particles on a radial course and a static electric quadrupole field to confine them. A complex potential is created by using ten high voltage electrodes for AEgIS. To cool down the particles sufficiently and to reach the required measurement precision for the gravitational acceleration of 1 %, a cryogenic environment with temperatures of about 100 mK is necessary in the Penning trap. For the production of antihydrogen $\bar{H}$ the next step is to produce positronium (Ps). It would be also possible to produce antihydrogen by mixing antiprotons with positrons, but this is a long-duration process. Furthermore, the production with positronium has the advantage of a pulsed production. Positronium consists of an electron-positron pair. These two can annihilate which causes the very short

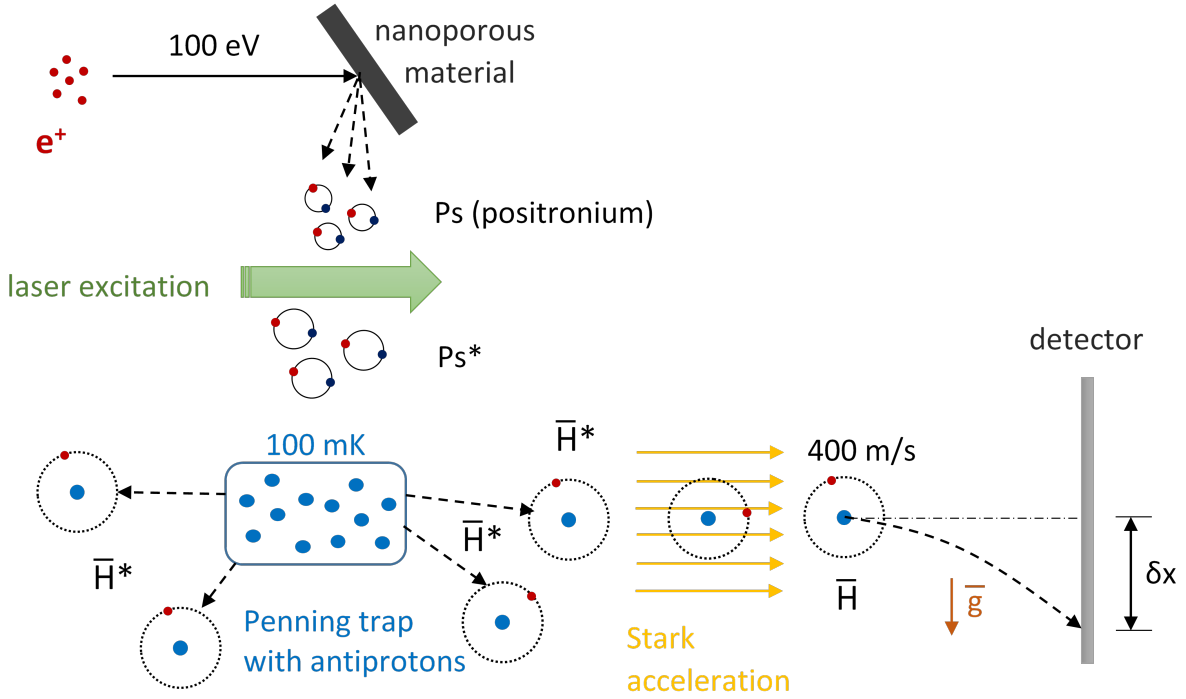

Figure 1.2: Schematics of the AEgIS creation of antihydrogen and its measurement procedure.

lifetime of positronium in the nanosecond range. Furthermore, the electron is strongly bound to the positron for positronium in its ground state. Therefore, the elements are excited by a laser to Rydberg states (n= 30 ... 40) where the positron and the electron are far apart from each other. At these exited states the binding energy is lower which makes recombination easier. The Rydberg positrons are guided in the Penning trap with the cooled antiprotons $\bar{p}$ where they can recombine by resonant charge exchange to antihydrogen. After formation of antihydrogen the exited atom can leave the Penning trap in a random direction. Neutral atoms cannot be accelerated in a constant electrical field. However, because of the dipole moment of these Rydberg atoms they can be accelerated by an electrical gradient field, called Stark acceleration. Antihydrogen is produced at velocities of 25...80 m/s and will be accelerated to about 400 m/s in the direction of the measurement set-up. The combination and measurement principle is shown in Figure 1.2. A detailed description can be found in [6, 7, 8].

1.2. Scope of the thesis

As stated at the beginning a milliKelvin environment in the Penning trap is necessary for the success of the experiment. Therefore, the high voltage electrodes need to be cooled

properly while withstanding electrical potentials up to 1 kV. Such low temperatures can be reached by a mixture of ^{3}He and ^{4}He in a so-called dilution refrigerator. The coldest part of the device is the mixing chamber. Because of the creation and annihilation of matter, the electrodes are exposed to short strong heat pulses, thus it is important that the electrodes are able to transport these heat loads as fast as possible to the mixing chamber. This ability can be described by the thermal diffusivity, defined as the ratio between the thermal conductivity and specific heat times density.
The diffusivity of bulk materials can be found in literature even down to the milliKelvin temperature range. Caused by the thermal link to the mixing chamber one has a special case - a sandwich consisting of different materials in the thermal pathway. Two designs exist for the connection from the electrode to the mixing chamber. Either a sapphire-indium (deposited)-indium (foil)-copper sandwich (S1) like proposed by T. Eisel [1] or a sapphire-titanium-gold-indium (foil)-copper sandwich (S2) like proposed by J. H. Derking et al. [9]. A detailed description can be found in section 3.3. The design proposed by J. H. Derking et al. is easier to establish, since the electrode is already sapphire coated with titanium-gold towards the cooling source and no special treatment of the connection area is required. But at ultra-low temperatures special attention has to be given to the thermal boundary resistance which may hinder the heat transfer.

To identify the best composition of the sandwich in terms of thermal diffusivity the following investigations are of vital importance:

(1) Investigation of the AC measurement method

The AC method is used to determine the thermal diffusivity. A sinusoidal heat load is applied on one side of the sample. Due to amplitude attenuation and phase shift along the sample the diffusivity can be calculated. The same method was already used by C. van der Post [10] to measure the thermal diffusivity of such a sandwich. These results were not explicit and showed a frequency dependence. Therefore, the method has to be validated.

(2) Diffusivity experiments at low temperatures of the sandwich designs

The measurements are performed in the temperature range from 3 K to 30 K and the temperatures are reached by a cryocooler. This investigation is important to understand the influence of the boundaries at low temperatures and to compare it to results obtained at ultra-low temperatures. Furthermore, literature data at low temperatures is accessible, which allows to validate the results and to gain some information for the modeling of the thermal performance of the sandwich structure.

(3) Diffusivity experiments at ultra-low temperatures of the sandwich designs

The measurements are performed between 30 mK and 300 mK, the electrode's final operating temperature range for application. These studies are used to investigate the increasing influence of the thermal boundary resistance at decreasing temperatures and to conclude the best sandwich design. In the milliKelvin temperature range some of the materials are superconducting. The studies include the analysis of the superconducting and normal conducting state. A magnetic background field will suppress the superconductivity of materials in AEgIS.

This work will first explain the fundamentals of heat transport in solids at low temperatures,focusing on the influence of composite structures, followed by a description of the different experimental set-ups including the working principle of a cryocooler and a dilution refrigerator describing the impact for the measurement of the electrode design and the resulting sandwich structures. Afterwards, the experiments performed on the reference samples and the sandwich structures in different temperature ranges are explained, the results are presented and a modeling of the measured values is discussed. Finally, a decision for the final sandwich design is made.

2. Heat transport in solids and across interfaces

2.1. Heat capacity of solids

The heat capacity provides a lot of information about a material and is a measure of how much energy is necessary to heat up a material, i.e. it is a measure of the excited states of a material at a specific temperature. The molar heat capacity at a constant volume C_v is defined in equation (2), where U is the internal energy and T the temperature and it has

$$C_v = \left(\frac{\partial U}{\partial T}\right)_V \quad . \tag{2}$$

The excitations in crystalline insulators like sapphire are phonons - discrete lattice vibrations. At high temperatures all lattice vibrations are exited, thus, the heat capacity is constant and can be described with equation (3) the Dulong-Petit law where k_B is the Boltzmann constant and N the number of particles per amount of substance

$$C_v = 3Nk_B = 24.9\frac{J}{mol \cdot K} \quad . \tag{3}$$

The approach is not valid at low temperatures, where the thermal energy ($k_BT \approx \hbar\omega_{ph}$) is too low to excite all phonons. The phonons begin to "freeze out". The corresponding

temperature is called Debye temperature Θ_D - the temperature where all states are occupied. The behavior of the molar heat capacity in the whole temperature range can be described by the Debye theory, which describes the phonons as a free Bose gas (elastic, isotropic, homogeneous continuum). With these assumptions one can predict the molar heat capacity in different temperature ranges in good agreement with the measurements. The molar heat capacity calculated from the Debye model for low and high temperatures compared with the experimental data is shown in Figure 2.1. It shows that at low temperatures ($T < \Theta/10$) the molar heat capacity decreases with T^3 according to equation (4):

$$C_v = \frac{12\pi^4}{5} N k_B \left(\frac{T}{\Theta}\right)^3 = \beta T^3 \quad . \tag{4}$$

In metals conduction electrons have to be taken into account. These fermions can be thermally excited and each energy state can be occupied by two electrons with anti-parallel spin up to the Fermi energy. At low temperatures the properties of metals are solely determined by electrons in energy states close to the Fermi energy [11]. To estimate the density of states one can use the "free-electron model", but for real metals electron-electron interactions, electron-ion interaction and the symmetry of the crystal have to be considered. This behavior can be described with the quasiparticle model where each electron has an effective mass m^*, i.e. the electron behaves "lighter" or "heavier" compared to a normal electron due to its interactions.

$$C_v = \gamma T + \beta T^3 \tag{5}$$

Equation (5) describes the behavior of the molar heat capacity for metals like copper at low temperatures. In this equation γ is the Sommerfeld constant. The electronic molar heat capacity becomes important below 10 K and is dominating below 1 K [11].

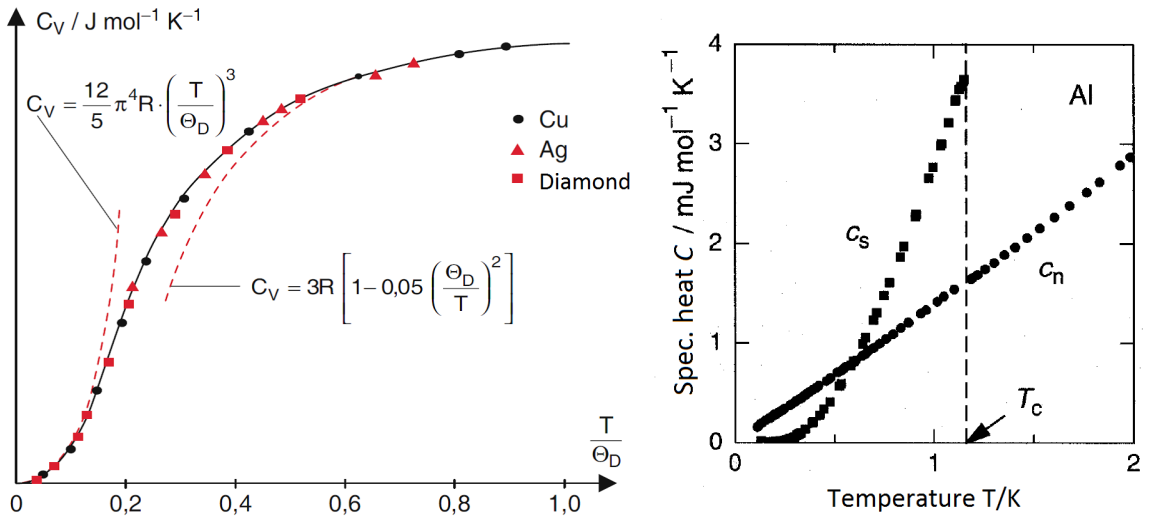

Figure 2.1: Molar heat capacity in Debye model (left) [12] and of aluminum in superconducting c_s and normal conducting state c_n (right) [13].

Superconductors near the transition temperature T_C reveal a different behavior shown in Figure 2.1 (right). The phonon molar heat capacity shows monotonic behavior, but the electronic molar heat capacity shows a jump at this second-order phase transition. The possibility of entering the superconducting state can be interpreted as an additional "degree of freedom" and leads to an increasing molar heat capacity. According to the Bardeen-Cooper-Schrieffer (BCS) theory, a microscopic theory of superconductivity that predicts many of the properties of elemental superconductors, a jump of the electronic molar heat capacity of $\Delta C = 1.43\ \gamma T_C$ occurs at the transition temperature [14]. For indium which becomes superconducting below $T_C = 3.4$ K a higher jump in electronic molar heat capacity of $\Delta C = 1.73\ \gamma T_C$ was measured [15]. At temperatures below T_C, the molar heat capacity decreases exponentially and results in a lower molar heat capacity in superconducting state than in normal conducting state at temperatures much smaller than T_C as illustrated in Figure 2.1 [13].

2.2. Thermal conductivity in solids at low temperatures

If a temperature gradient exists between two solids, these systems transfer heat until the equilibrium is reached. The three mechanisms to transfer heat are conduction, convection and radiation. Heat transfer in solids is dominated by thermal conduction where energy is exchanged between adjoining atoms and molecules. This behavior is accomplished in insulators by lattice vibrations and in metals additionally by the free electrons. It can be characterized by the thermal conductivity coefficient λ. In general the parameter results from the multiplication of specific heat c_v at constant volume, mean free path l, density ρ and velocity of the heat carriers v shown in equation (6). A multiplication factor of $1/3$ expresses the heat flow in one direction [16]:

$$\lambda = \frac{1}{3} \cdot c_v \cdot \rho \cdot l \cdot v \quad . \tag{6}$$

For heat transport performed by phonons v is the velocity of sound and l the mean free path of the phonons. The mean free path of the phonons is determined by scattering on crystal faces, lattice defects, amorphous structures and phonon-phonon scattering. In monocrystalline sapphire the distances between lattice defects are very large, so the phonon-phonon scattering is the limiting factor for the thermal conductivity at high temperatures. At low temperatures the phonon-phonon scattering decreases while their mean path increases until it has reached the size of the defects distance. At that point the mean free path is independent of temperature. If the mean free path reaches the range of the lateral dimensions of the sample the only temperature dependent quantity is the specific heat, which decreases with T^3 at low temperatures. Due to this behavior the thermal conductivity for almost ideal crystals has a maximum at around $\Theta_D/30$. At low temperatures monocrystalline crystals like sapphire ($\lambda = 6500$ W/Km) can reach even higher

thermal conductivity than metals [16].
In general, metals are good thermal conductors because they have free electrons for the energy transport, in addition to the phonons. The Fermi velocity of the conduction electrons is much higher than the acoustic velocity of the phonons, which also increases the thermal conductivity [11]. These electrons can be scattered on lattice defects and at higher temperatures with phonons. In pure metals the electron contribution to the heat transport dominates at all temperatures. One can calculate the thermal conductivity with equation (6) as well. In that case v is the mean velocity due to thermal movement and l the mean free path of the electrons. For high temperatures $T \gg \Theta$ one gets a constant thermal conductivity because the mean free path caused by impacts is proportional to $1/T$ and the specific heat is proportional to T. At low temperatures $T \ll \Theta$ the mean free path of the electrons increases ($\lambda \sim T^{-2}$) until it reaches the dimension of the lattice defect distance and stays constant [16]. At these temperatures the specific heat and consequently the thermal conductivity are proportional to temperature ($\sim T$). The purity of the materials is responsible for the temperature and the value of the maximum in thermal conductivity cf. [16, 17].
In superconductors one observes a difference in thermal conductivity at the same temperature in superconducting and normal conducting state. This is attributed to the fact that the type of heat carriers changes in superconductors at T_c by the formation of Cooper pairs [11]. These Cooper pairs do not interact dissipative with the lattice, i.e. they do not transport heat. Some electrons which contribute to the heat transport in normal conducting state are now bound in Cooper pairs and this decreases the thermal conductivity in the superconducting state [16, 17]. The process is more complex for materials with impurities and for some alloys the thermal conductivity is even higher in superconducting state than in normal conducting state (e.g. Pb + 10 % Bi) [15].
The thermal conductivity of a material can be investigated by steady state measurements with a known applied heat load. Local and transient temperature behavior in a material can be described with the heat equation, a parabolic partial differential equation shown in equation (7):

$$\bigtriangledown^2 T = \frac{1}{D} \cdot \frac{\partial T}{\partial t} \quad . \tag{7}$$

In case of a constant heating of a homogeneous isotropic body with two parallel sides and with the heat load $\dot{Q}$ it follows, after a thermalization time, a constant temperature gradient ΔT between the parallel sides. The time dependent part of the equation dissolves and one can easily calculate the thermal conductivity with equation (8) considering the sample's geometry where A is the area the heat flows through and l the distance between the parallel walls [18]

$$\lambda = \frac{\dot{Q} \cdot l}{A \cdot \Delta T} \quad . \tag{8}$$

2.3. Thermal resistance at material boundaries

At low temperatures one has to pay attention to the boundary resistance at interfaces of materials. Stacking materials in series can lead to a lower thermal conductivity than expected from adding up the individual parameters for each material. This is attributed to the thermal boundary resistance, which decreases the overall thermal conductivity of a stack. Thermal boundary resistance was first described for interfaces between solids and liquid helium (Kapitsa resistance) [19]. It affects for example the heat transfer between the parts of a dilution refrigerator (heat exchangers, mixing chamber). Also at solid-solid interfaces thermal boundary resistance occurs. Here, the thermal boundary resistance is highly influenced by the actual contact area between the boundaries, which at interfaces of metals can often be only 10^{-6} of the nominal area [11].

2.3.1. Thermal boundary resistance between liquid helium and solids

Pyotr Kapitsa was the first who reported a significant temperature drop at the liquid helium-solid boundary in 1941 [20]. For this thermal boundary resistance, Khalatnikov presented in 1953 the first model - the acoustic mismatch model (AMM) - which predicts the thermal boundary resistance below 100 mK in good agreement with measurements [19].

The acoustic mismatch model claims that not all phonons which reach the interface are transmitted, due to the different acoustic properties of the material, refraction and acoustic impedance occur. The simplifying assumptions in the model are, that it treats the interface as a plane, the phonons as plane waves and the material in which the phonon propagates as continuum. In solids the speed of sound is typically around $v_s = 3000$ m/s and in ^{4}He $v_{He} = 238$ m/s [13]. The critical angle α_c, above which total reflection of the phonons occurs, can be calculated with the "Snell's law" and is, in case of an solid-helium interface:

$$\alpha_c^{He\to s} = arcsin(v_{He}/v_s) \approx 4^\circ \quad , \tag{9}$$

$$f_c^{He\to s} = \frac{1}{2} sin^2(\alpha_c^{He\to s}) \quad . \tag{10}$$

The number of phonons reaching the interface within the critical angle is less than 1% and can be estimated by equation (10). Caused by the acoustic impedance only a small number of these phonons are transmitted in the solid. The acoustic impedance $Z_i = \rho_i v_i$ is the product of mass density and the phonon velocity. The resulting energy transmission probability t is described in equation (11) for the condition $Z_s \gg Z_{He}$:

$$t^{He\to s} = \frac{4 \cdot Z_s \cdot Z_{He}}{(Z_{He} + Z_s)^2} \approx \frac{4 \cdot Z_{He}}{Z_s} \quad . \tag{11}$$

At the boundary between liquid helium and copper $t^{He\to s}$ is approximately 10^{-3} [13].

Combined with the probability for reaching the boundary within the critical angle $f_c^{He\to s}$, one gets a total transmission probability of $\approx 10^{-5}$. That of course hinders the heat transport between different materials.
The thermal boundary resistance is defined as shown in equation (12) where ΔT is the steady-state difference between the surface temperature on each side and the heat load is $\dot{Q}$:

$$R_K = \frac{\Delta T}{\dot{Q}} \quad . \tag{12}$$

The heat flow $\dot{Q}$ by phonons impinging on the interface is T^4 dependent and can be calculated with the following equation (13) for a liquid helium/solid boundary [11]:

$$\dot{Q} = \frac{A \cdot k_B^4 \cdot \pi^2 \cdot T^4 \cdot \rho_{He} \cdot v_{He}}{30 \cdot \hbar^3 \cdot \rho_s \cdot v_s^3} \quad . \tag{13}$$

At an interface with $T_{He} \neq T_s$ and a temperature difference $\Delta T \ll T$ the transported heat load can be described with the following equation:

$$\dot{Q} = \frac{d\dot{Q}}{dT}\Delta T = \frac{2 \cdot A \cdot k_B^4 \cdot \pi^2 \cdot \rho_{He} \cdot v_{He}}{15 \cdot \hbar^3 \cdot \rho_s \cdot v_s^3} \cdot T^3 \Delta T \quad . \tag{14}$$

If one inserts equation (14) in equation (12) it leads to a T^{-3} dependence for the thermal resistance, thus, the Kapitsa resistance becomes more important with decreasing temperature:

$$R_K = \frac{15 \cdot \hbar^3 \cdot \rho_s \cdot v_s^3}{2 \cdot A \cdot k_B^4 \cdot \pi^2 \cdot \rho_{He} \cdot v_{He} \cdot T^3} \quad . \tag{15}$$

Frequently discussed in literature is the Kapitsa resistivity R_k which can be calculated with the following equation for a temperature difference rather high compared to the absolute temperature [21]:

$$R_k = \frac{A}{4\dot{Q}} \left(T_{hot}^4 - T_{cold}^4\right) \quad . \tag{16}$$

Plotted versus temperature R_k should be constant between 10 mK and 100 mK. At higher temperatures where the temperature difference is rather small compared to the absolute temperature the thermal resistivity is calculated with the following equation [21]:

$$R_k = \frac{A}{\dot{Q}} T^3 \left(T_{hot} - T_{cold}\right) \quad . \tag{17}$$

The acoustic mismatch model predicts the thermal boundary resistance between solids and liquids in good agreement with experimental data at temperatures below 100 mK [19]. At increasing temperatures the thermal boundary resistance drops and becomes much smaller than predicted by the acoustic mismatch model. The measured results are then closer to the boundary resistance predicted by the diffuse mismatch model (DMM) suggested by E. T. Swartz [19].
The diffuse mismatch model predicts significant lower thermal boundary resistance at

liquid helium/solid interfaces caused by the fact that it considers scattering effects, which opens new channels for heat transport. Phonons are scattered diffusely at the interface and it is assumed that the scattered phonon "forgets" where it came from. That makes the probability of a phonon entering another material independent from where it came from. The probability becomes proportional to the density of phonon states into which the phonons can scatter. Considering a phonon coming from copper and reaching a liquid helium boundary it will immediately forward scatter into liquid helium. The density of phonon states is proportional to ω^2/v^3 [19]. As seen before the phonon velocity in liquid helium is approximately one order of magnitude smaller than in most solids. Subsequently, the density of low-frequency phonon states in liquid helium is much higher than in solids. The effect can decrease the Kapitsa resistance predicted by the DMM compared to the AMM by two orders of magnitude. According to the AMM the phonon would be reflected on the interface due to the different acoustic properties of the materials [19].
Figure 2.2 schematically shows the process described in acoustic and diffuse mismatch model for a boundary between helium and solid. The left picture illustrates the acoustic mismatch model with the acoustic impedances Z at the interface, the incidence and emergent angle α of a phonon and the critical cone, determined by the three dimensions of the critical angle. The right picture describes the processes at an interface according to diffuse mismatch model with the reflection $r(\omega)$ and transmission probabilities $t(\omega)$ at the boundary determined by the density of phonon states. In the model are no physical restrictions for the scattering mechanism made and it exists no dependency on the interface properties [22].

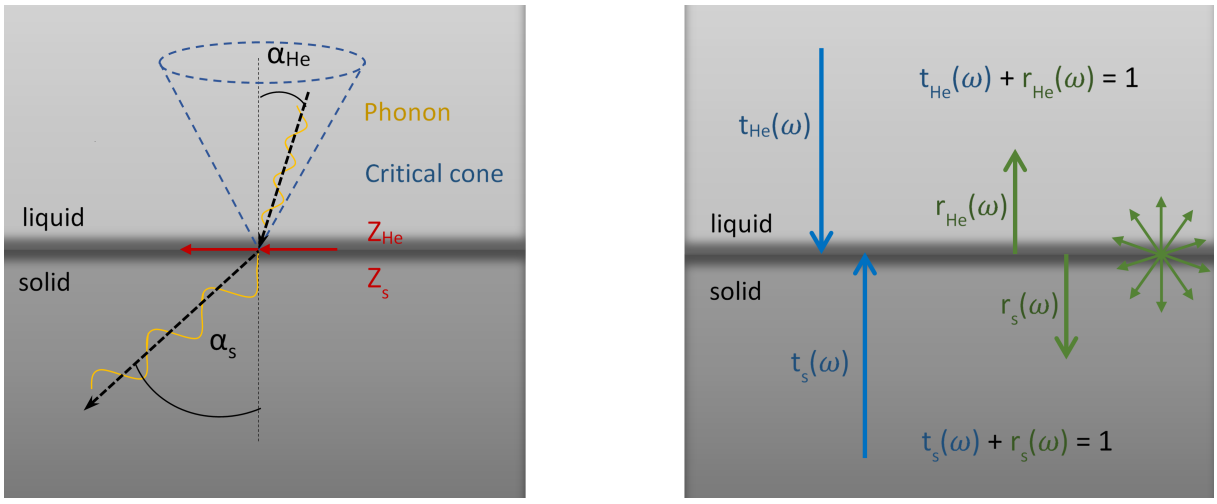

Figure 2.2: Accoustic mismatch (left) and diffuse mismatch model (right) cf. [22].

2.3.2. Thermal resistance at boundaries between solids

Thermal boundary resistance caused by the acoustic properties also appears at solid-solid interfaces. For similar solid/solid boundaries the acoustic mismatch is much smaller than

at the interface of liquid helium and a solid. Thus, approximately half of the scattered phonons are transmitted in the other material [19]. In terms of the DMM for a solid/solid boundary with the same transverse phonon velocities the transmission probability is exactly 50 %. That means the difference between the acoustic and diffuse mismatch model is smaller for solid-solid interfaces with similar acoustic properties [19].
The acoustic mismatch model was extended for solid/solid boundaries in 1959, but measurements showed that the boundary resistance between two solids was often higher than predicted and the measurements had a poor reproducibility [19].
The difference can be explained by the fact, that only a fraction of the surface area is in physical contact due to the surface roughness. The materials do not touch completely at the interface [23]. The contact area can vary depending on material and surface treatment. This implies that a mechanical force close to the yield strength, which presses the interfaces together, can increase the contact area [11]. Thus, the thermal boundary resistance can be decreased. T. Okamoto et al. reported in [24] a very low electrical contact resistance (10 nΩ at 4.2 K) at a gold-plated copper/copper interface, which were bolted together (4 Nm). The electrical resistance is connected to the thermal resistance by the Wiedemann-Franz law [25]. A possible disadvantage of the method is the lattice deformation.
The thermal contact at metal interfaces can be further increased by interposing a soft ductile material with high conductivity such as indium foil or by applying grease in between the interfaces and pressing them together. Salerno et al. reported in [26] that this can improve the results up to one order of magnitude.
Also a surface treatment like polishing can improve the conductivity at interfaces. T. Eisel showed for a dielectric/metal boundary in [1] a decrease of the thermal boundary resistance due to polishing of the sapphire surface.

2.4. Thermal diffusivity

2.4.1. Definition

The thermal diffusivity D is a material parameter for the dynamic behavior of a bulk material. It describes the change in time of the spatial temperature distribution caused by a temperature gradient. Thermal diffusivity is defined as thermal conductivity divided by the specific heat c times the density ρ as shown in equation (18) and has the unit $\mathrm{m^2/s}$:

$$D = \frac{\lambda}{c \cdot \rho} \quad . \tag{18}$$

The behavior of thermal conductivity and specific heat at low temperatures was already discussed. At temperatures below the maximum the thermal conductivity decreases with T^3 in insulators because the mean free path is in the range of the lateral dimensions. In that case the specific heat is the only temperature dependent quantity left. The same

happens in metals when the mean free path of the electrons reaches the dimension of the lattice defects, the temperature behavior is the same as that of the heat capacity. Since one divides the thermal conductivity by the heat capacity, the thermal diffusivity should become constant when the described conditions are fulfilled. As stated at the beginning, the thermal diffusivity is a parameter defined only for bulk materials. How fast a heat disturbance travels from one point of a sandwich made of different materials in series, depends also on the boundaries. The propagation speed of the temperature wave is different in each layer and the resulting diffusivity for a sandwich can be named as D_s. The thermal diffusivity for a stacked material should have a T^3 dependence at ultra-low temperatures. For a bulk material all temperature dependent factors vanish after the above described point. In a stacked material, after the mean free path of the heat carrier reaches the lateral dimensions, the only temperature dependent quantity left is the thermal boundary resistance. So instead of only adding up the parameters for each material in series, one has to add an additional resistance for the boundaries, which decreases the thermal diffusivity. For a sandwich consisting of many layers one gets equation (19):

$$R_s = \sum_i R_i + \sum_j R_{K_j} \quad . \tag{19}$$

Where R_{K_j} is the thermal boundary resistance as defined in equation (12). The thermal resistance caused by the material itself R_i can be calculated from the thermal conductivity considering of its dimensions as shown in equation (20), where A is the cross section through which the heat is transported and x_i is the thickness of each layer:

$$R_i = \frac{x_i}{\lambda_i \cdot A} \quad . \tag{20}$$

The total specific heat capacity multiplied by the density for a whole sandwich structure of a constant cross section can be determined by adding up the specific heat capacity c_i times the density ρ_i for each layer and multiplied by the percentage of the total thickness of the layer. This is shown in equation (21), where d is the total thickness of the whole sandwich:

$$c_s \cdot \rho_s = \sum_i \frac{x_i}{d} \cdot c_i \cdot \rho_i \quad . \tag{21}$$

An effect caused by the boundaries which changes the heat capacity significantly for a sandwich is not known. Jun reports in [27] that the film thickness of Al can influence the heat capacity for a temperature range from 300 K to 420 K. A small film thickness enhances the heat capacity, but for a layer thickness of 1150 nm the reported specific heat is the same as for the bulk material.

The thermal diffusivity of a sandwich structure with different materials in series can be calculated with equation (22). Therefore, equation (18) to equation (21) are combined to:

$$D_s = \frac{d}{A \cdot R_s \cdot c_s \cdot \rho_s} \quad . \tag{22}$$

2.4.2. AC method to determine thermal diffusivity

A common method to determine the thermal diffusivity of a material is the AC method, which uses a sinusoidal heat signal. The temperature modulation is applied to one side of a sample with two parallel sides. By crossing the sample the temperature wave gets attenuated and phase shifted. The magnitude of attenuation and phase shift can give information about the thermal diffusivity of the sample. Therefore, the differential heat equation (7) has to be solved. For heat flow only in one dimension the equation simplifies to equation (23):

$$\frac{\partial^2 T(x,t)}{\partial x^2} = \frac{1}{D}\frac{\partial T(x,t)}{\partial t} \quad . \tag{23}$$

The partial differential equation can be solved by the "separation of variables" -method, which assumes the solution can be described by the product $T(x,t) = X(x) \cdot Y(t) + C$. This results in equation (24) and has to be constant (δ^2), as it has to be valid at all places and times:

$$\frac{1}{X}\frac{\partial^2 X}{\partial x^2} = \frac{1}{D \cdot Y}\frac{\partial Y}{\partial t} = \delta^2 \quad . \tag{24}$$

The resulting two differential equations can be easily solved and one gets equation (25):

$$T(x,t) = X_0 \cdot Y_0 \cdot e^{D \cdot \delta^2 \cdot t + \delta \cdot x} \quad . \tag{25}$$

Solving the equation for a modulated temperature signal and the boundary condition for $x = 0$ and $x = \infty$ gives the final solution:

$$T(x,t) = T_m + A \cdot cos\left(\omega t - \frac{x}{\mu}\right) \quad , \tag{26}$$

where T_m is the mean temperature and A the amplitude of the temperature oscillation. The oscillation is generated with a constant period T_{per} and the resulting angular frequency $\omega = 2\pi/T_{per}$. The thermal diffusion length μ gives the distance at which the amplitude of the temperature wave reduces e times from the amplitude at the stimulated surface [28]. The thermal diffusion length can be calculated from the phase shift or amplitude ratio between the initial signal and the signal after passing the sample. Both methods allow the calculation of the thermal diffusivity from these values [29]:

$$\mu = \frac{x}{\varphi(x) - \varphi(0)} = \frac{x}{ln\left(\frac{A(0)}{A(x)}\right)} = \sqrt{\frac{2 \cdot D}{\omega}} \quad . \tag{27}$$

In equation (27) $\phi(0)/A(0)$ equal the phase/amplitude of the initial wave and $\phi(x)/A(x)$ the phase/amplitude of the temperature oscillation after crossing the sample. A typical measurement signal is given in Figure 2.3. The initial signal $T(x = 0)$ is illustrated in red and has a higher amplitude. The phase shifted and attenuated signal $T(x = d)$ is illustrated in blue.

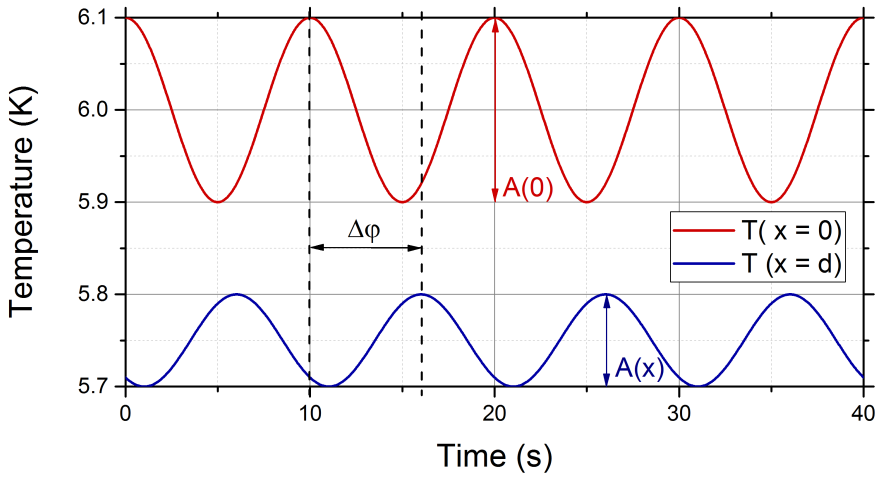

Figure 2.3: Typical measurement signal using AC method showing different amplitude ratios and phase shift between initial and attenuated signal.

3. Experimental set-ups

3.1. Cryocooler principle

Nowadays, the use of cryocoolers instead of evaporating liquid cryogens for cooling is quite common. Many different cryocooler types have been developed over the years, reaching different temperature ranges [30]. The advantages of cryocoolers are the comparably high efficiency, long lifetime, low noise, low price and the small size providing the cold source directly in the insulation vacuum. Depending on the requirements of the experiment, it has to be decided if the usage of cryocoolers is suitable as they may cause mechanical vibrations, electromagnetic interferences and temperatures variations (for regenerative cryocoolers) [31], that may influence the measurement.

To generate the temperature range of 3 K to 30 K for the thermal diffusivity measurement of the different sandwich designs, a two-stage pulse tube refrigerator that can deliver up to 1 W of cooling power at 4.2 K is used. The basic elements of the used pulse-tube cryocooler are illustrated in Figure A.1 (left) where q is the heat flow and T is the temperature. The helium gas inside the cold head is subject to an adiabatic compression and expansion cycle. The necessary phase shift to generate a cooling power is due to the phase difference of the main piston (mostly replaced by a compressor + valve unit) and the RC function of the reservoir and the inertance tube. Hence, a cooling power is provided at the cold stage. Due to the operating cycle a mechanical vibration in the 10th of µm and a temperature oscillation present at the cold stage interface of about ± 0.5 K for two stage cryocoolers. Details can be found in [17, 30, 32].

Pulse-tube cryocoolers show oscillations of the refrigeration temperature that result from

the pressure changes of the working fluid. In thermal diffusivity studies, where thermal oscillations in the milliKelvin range are used, the temperature oscillations might be disturbing and need to be damped. G. Dubuis et al. in [33] introduced a method to dampen temperature oscillations to less than 1 mK without reasonable increase of the base temperature and reduction of the cooling power. The thermal damping system is shown in Figure A.1 (right) and consists of thin sheets of lead (dark gray), stainless steel (white), and copper (red). Lead was chosen because of its high specific heat and relatively high conductance at low temperatures. Thus, a small volume generates a high total heat capacity. To increase the thermal conductance of the damper a copper ribbon folded in zigzag manner in-between the lead discs was used and the stainless steel plate is for stabilization and serves as a thermal insulator of the stack. The described buffer acts as the heat transfer link between the experimental set-up and the cold head as a low pass filter and increases the thermal stability of the experimental set-up significantly, see Figure 3.1.

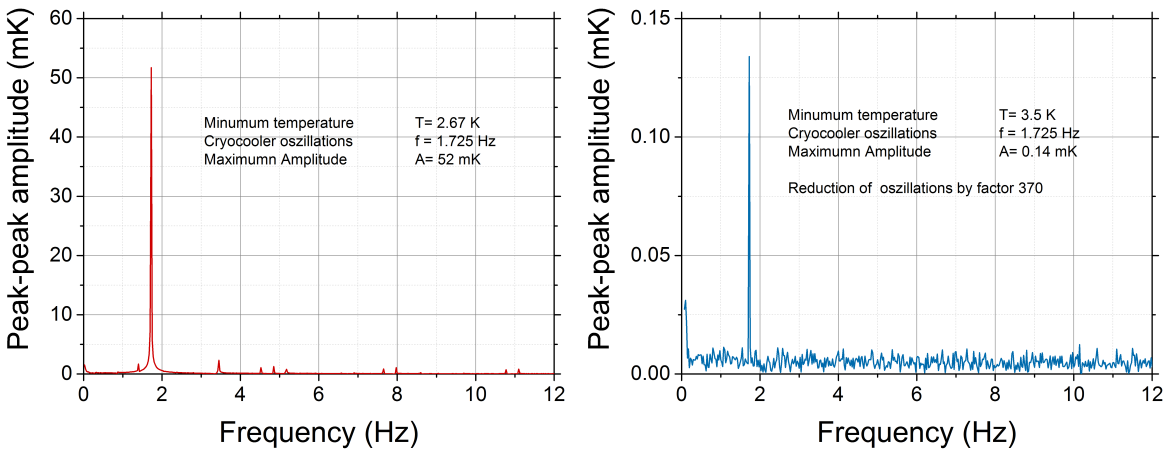

Figure 3.1: Plot of the measured peak-peak cryocooler oscillations versus frequency without the damper (left) and with damper (right). The damper reduced the amplitude of the oscillations by a factor of 370.

The CERN Cryolab pulse-tube refrigerator is shown in Figure 3.2 and has two cold stages. The temperature of the two cryocooler stages depends on the applied heat loads. To individually control the temperature, heaters are attached to both stages of the cryocooler. The 1st stage is used to thermally anchor the cables coming from the measurement devices and to minimize heat loads by radiation reaching the 2nd stage. Therefore, a thermal shield of polished copper covered by multi-layer insulation (MLI) is attached to the 1st stage. The coldest part of the refrigerator, reaching about 2.7 K, is the 2nd stage. It is used for further thermal anchoring of the cables coming from the devices and can be heated to the temperature required by the experiment. The experimental platform is either directly coupled to the 2nd stage for best thermal contact or a G10 fiberglass plate

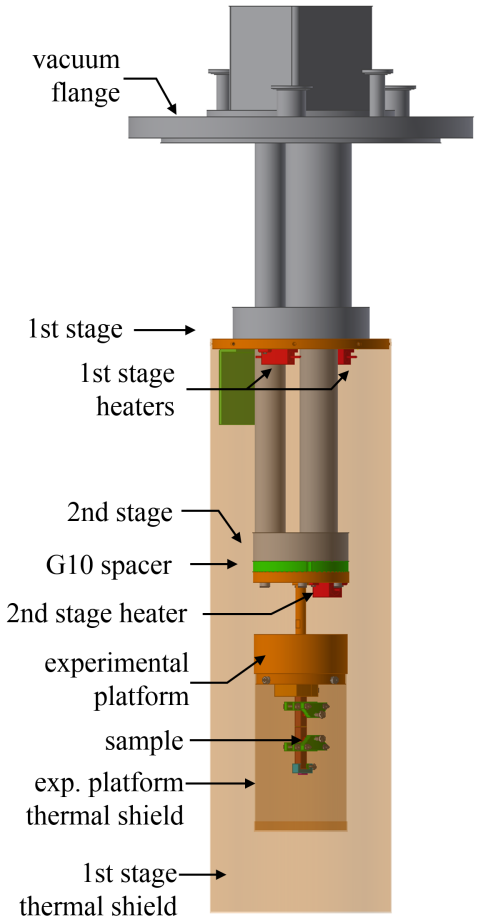

Figure 3.2: Schematics of the CERN Cryolab two-stage pulse-tube refrigerator [34].

can be inserted in between the cold head and the platform allowing experiments at higher temperatures. Instead of the G10 plate it is also possible to insert the described damper for thermal stabilization of the measurement. The experimental platform has also a copper thermal shield wrapped in MLI [34]. The whole insert is placed in a vacuum chamber providing the required insulation vacuum of $p < 10^{-7}$ mbar. The low temperature measurements of the thermal diffusivity and thermal conductivity (used for the modeling) for both sandwich stacks are performed in this experimental set-up.

3.2. Dilution refrigerator principle

As discussed before, temperatures around 100 mK are necessary in the Penning trap of AEgIS. These temperatures can be achieved by a dilution refrigerator (DR), which takes advantage of the properties of a mixture of ^{3}He and ^{4}He. The phase diagram of the mixture is shown in Figure 3.3. It can be seen that ^{4}He becomes superfluid below $\sim$ 2.177 K while ^{3}He becomes superfluid in the low milliKelvin range. If liquid ^{4}He is diluted with ^{3}He the temperature for the phase transition decreases. This is depicted in the phase diagram with the Lambda line, see Figure 3.3 (left). For a mixture of more

than 67.5 % ^{3}He the liquid does not become superfluid at any temperature and below 867 mK the lambda line meets a phase-separation line. At temperatures below this point the isotopes can only mix at certain concentrations depending on the temperature. The two phase region is a forbidden area, where a mixture of the two fluids is not possible in the given ratio, hence, a concentrated and a diluted ^{3}He phase emerge. The diluted phase has a minimum concentration of 6.6 % ^{3}He. The concentrated phase is almost pure ^{3}He at ultra-low temperatures and floats above the diluted phase due to its lower density. The concentration of ^{3}He in the diluted phase is even the same at temperatures approaching zero and the fluid does not exsolve completely. The reason for the mixture ratio is, that the binding energy between the ^{3}He atoms is smaller than between ^{3}He and ^{4}He atoms. The system is at this ratio in equilibrium. That fact can be used for cooling by pumping on the diluted phase. To keep the concentration ratio while pumping, ^{3}He atoms will move from the concentrated phase into the diluted phase. For the phase transition, energy is necessary that will be removed from the environment [11, 13]. The

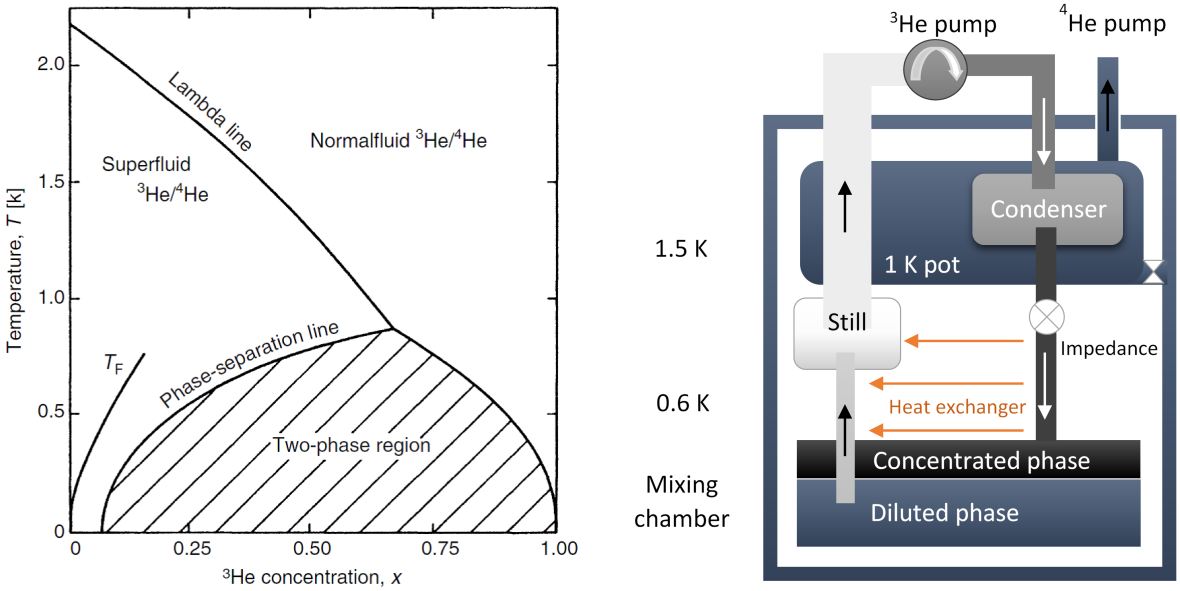

Figure 3.3: Phase diagram of helium mixture [11] (left) and dilution refrigerator principle (right).

^{3}He/^{4}He cooling circuit is shown in Figure 3.3 on the right side. The mixing chamber with the two phases of the mixture is embedded in a vacuum chamber surrounded by a ^{4}He bath for thermal insulation. The mixing chamber is the coldest point of the system at about 20 mK for the Cryolab DR. The diluted phase contains 6.6 % of ^{3}He and the ratio is kept by pumping on the still. The pumping generates an osmotic pressure which evokes a flow of the diluted phase towards the still through heat exchangers and heats the liquid up to 600 mK. The amount of liquid ^{3}He in the still is below 1 %, because of the different saturation pressures of ^{3}He and ^{4}He. Thus, almost only ^{3}He is pumped out at

these temperatures. Afterwards, the ^{3}He gas is cleaned outside of the cryostat in liquid nitrogen traps. After cleaning it enters the vacuum chamber again in the helium bath. In the 1 K pot it is pre-cooled down to 1.5 K. By using an impedance the pressure is kept high in the condenser so that the ^{3}He gas condenses. Afterwards, ^{3}He enters a heat exchanger for further cool down and enters at the end the concentrated ^{3}He phase in the mixing chamber. The CERN Cryolab dilution refrigerator is able to provide a continuous cooling power of 100 µW at 50 mK at the top lid outside the mixing chamber.

3.3. Sandwich design

The multi-layered composition foreseen for AEgIS between the electrode and the mixing chamber lid, makes a measurement of the thermal performance of metal-dielectric interfaces necessary. In order to investigate the thin layer effects and the influence of additional boundaries a mock-up sample of the multi-layer sandwich was built for measurements of the thermal diffusivity at different temperatures, see Figure 3.4. The material layer composition at the interfaces is defined by the electrode, which has to fulfill the following requirements of the final experiment in AEgIS.
The electrodes have to be made out of radiation hard materials and have to be suitable for ultra-high vacuum $< 10^{-12}$ mbar. Heat loads coming from cabling and thermal radiation make it necessary to have a good thermal contact to the heat sink. Due to the annihilation of antimatter, strong heat pulses are expected. Each 100 seconds a new bunch of particles arrives. One can predict a pulse of 10^{-5}J for 1 µs. This would be equivalent to 10 W at 100 mK. Assuming the pulse spreads over time one gets a heat load of about 10 µW in a time scale of 1 s.
Each electrode will be independently charged and discharged with up to $\pm$ 1 kV. Therefore, the electrodes have to be electrically insulated from the neighboring electrodes and from ground potential. As shown in section 2.2 heat transfer in insulators is carried out by phonons, exclusively. Phonons can scatter on defects in the lattice, which would decrease the thermal performance. In order to guarantee the best possible heat transport, the material has to have as few imperfections in the lattice as possible. A material that fulfills these demands is sapphire, a monocrystalline dielectric material [1]. Based on these requirements the electrode structure itself consists of a polished sapphire base covered with a 50 nm adhesion layer of titanium and a 750 nm thick gold layer forming the electrode [9]. Sapphire provides the electrical insulation of the of the electrical potentials.
The electrode design is shown in Figure 3.4 (left). To generate the electrical quadrupole field, ten of these shaped electrodes are placed in a row, where each ring electrode has a different potential. The electrodes are created by sputtering gold on a sapphire base in such a way that the passing particles have only gold in the direct line of sight. The important region in terms of heat transfer between electrodes and mixing chamber is marked

in purple. Heat flows from the electrode at a temperature of 100 mK down to the mixing chamber which is at 50 mK. The purple area needs to have good thermal contact to the top lid of the mixing chamber. The two different designs for the interface were already introduced in section 1.2. These sandwich designs are illustrated in Figure 3.4 (right). All experimental studies have been carried out with the sandwich mock-up.

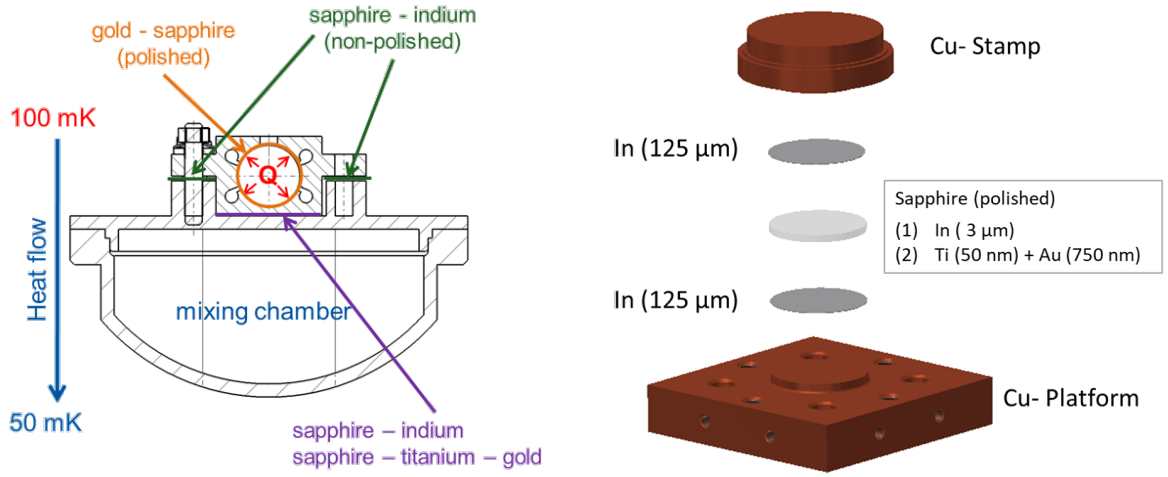

Figure 3.4: Electrode design mounted on the mixing chamber lid (left) [35] and sandwich design (right) [36].

(1) Sapphire-In-Cu (S1) configuration

T. Eisel already showed in his work [1] that a polished sapphire plate with 3 µm deposited indium has the lowest thermal resistivity, compared to non-polished and no indium deposited samples. The polishing reduces the surface roughness and enables better contact between the materials.
As seen in subsection 2.3.2, applying a pressing force and using a soft ductile material like indium can increase the contact between two metals by orders of magnitude. The sandwich design based on these observations consists of a 3 µm vapor deposited indium layer on a polished sapphire base. An indium foil of 125 µm thickness is placed between the copper platform and the indium deposited sapphire. The sandwich structure is pressed with about 10 kN, which is advantageous to create a "cold weld" between the two indium layers by exceeding the yield limit of indium.
The thermal diffusivity of the sandwich was already studied at ultra-low temperatures by T. Eisel et al. [37]. He claimed a dependence of the thermal diffusivity on the measurement frequency for the samples that were indium vapor deposited. The thermal diffusivity decreases with decreasing temperature and is over 6 orders of magnitude lower than the thermal diffusivity of the bulk materials used for the sandwich. His results are shown in Figure 3.5.

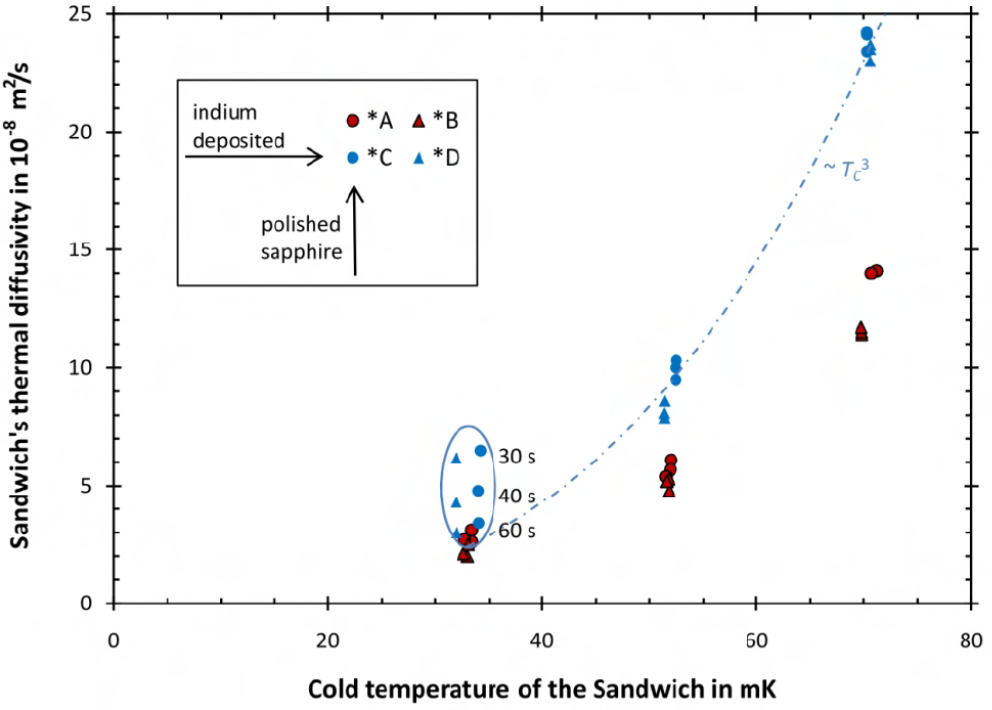

Figure 3.5: Diagram of the measured and simulated thermal diffusivity versus the cold temperature of the sandwich for the samples A, B, C, D (explanation see Figure 3.6). The periodic time is either 30 s, 40 s or 60 s, reprinted from [1].

Additionally, C. van der Post also studied the same sandwich in terms of thermal diffusivity at ultra-low temperatures [10]. He also claimed a dependence on the measurement frequency, which was not fully understood and is the reason for the importance of further investigations.

(2) Sapphire-Ti-Au-In-Cu (S2) configuration

As mentioned before the sandwich consists of 750 nm gold sputtered on a sapphire base. Since gold does not stick very well to sapphire, an adhesion layer of 50 nm titanium was added first. Using titanium-gold can save a step in the production of the electrode, since the whole sapphire electrode is already gold sputtered, so no additional treatment with vapor deposition of indium would be required. Again a 125 µm-thick indium layer is placed between the copper platform and the electrode to compensate mechanical imperfections of the copper geometry. Finally, the whole structure is pressed for better mechanical contact of the disk with about 10 kN.
That configuration had not yet been studied in terms of thermal diffusivity, but J. H. Derking et al. investigated the total thermal conductivity of the real size electrode connected to the mixing chamber of a dilution refrigerator at ultra-low temperatures [9]. It was expected that the deposited gold layer, just as the deposited indium layer, would decrease

the thermal interface resistance. Unfortunately, the thermal resistance found to be much higher than expected from the measurements performed by T. Eisel. J. H. Derking's results in comparison to the measurements of T. Eisel are shown in Figure 3.6. At the indium-gold interface free electrons are the main heat carriers, contributing substantially to the thermal contact of the metal layers. The sapphire base structure was subjected to high mechanical stresses (one sample broke during mounting). These high mechanical stresses, approaching the ultimate stress limit of sapphire, can be responsible for the increase of the overall thermal resistance [9]. Moreover, the additional boundaries of the thin titanium and gold films can be responsible for the increase in thermal resistance. This needs to be studied on a sandwich mock-up in terms of thermal resistance (done by J. Liberadzka) and also the effect of the additional boundary on the thermal diffusivity.

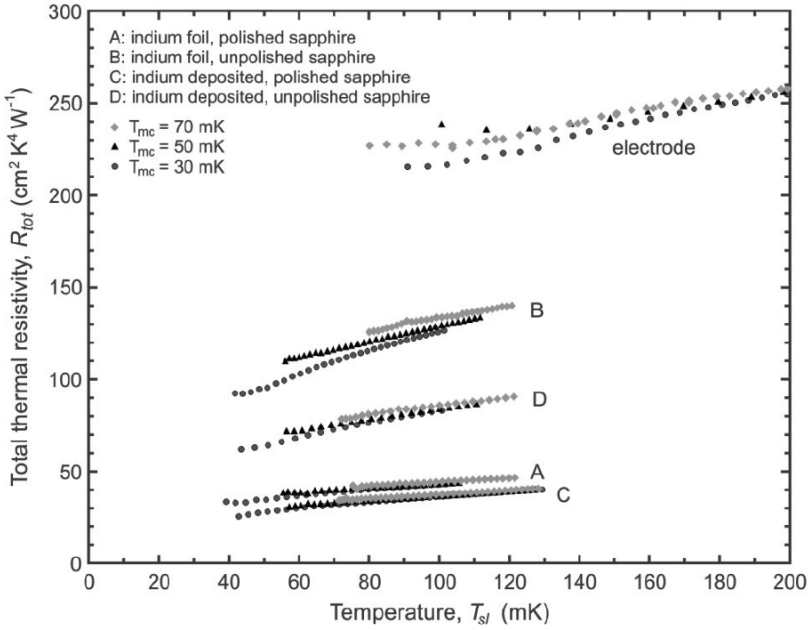

Figure 3.6: Total thermal resistivity of different sandwich designs measured by T. Eisel and of the high-voltage electrode measured by J. H. Derking versus the electrode temperature (T_{sl}) for different mixing chamber temperatures (T_{mc}) from [9].

As mentioned before both sandwich designs were compressed (F = 10 kN) by four bolts to create a "cold weld" between the indium layers. J. Liberadzka showed in her work [38] for an indium deposited sandwich in normal conducting state, that the difference in thermal performance with and without compressing force during the measurement is rather small when the "cold weld" was already established. On the basis of these results the sandwich designs studied in this thesis will be measured without compressing force.
To understand the complex structure and how fast it conducts heat, its thermal diffusivity

needs to be experimentally characterized in different temperature ranges. The thermal diffusivity is measured at low temperatures between 3 K and 30 K, where due to the fact that sapphire approaches its maximum in thermal conductivity between 30 K and 40 K, a maximum in thermal diffusivity of the sandwich is expected. The temperature range between 3 K and 30 K is used in order to gain information for the modeling of the sandwich structure. Furthermore, measurements will be done at ultra-low temperatures (30 mK - 300 mK) at which the electrodes will operate later. At these temperatures, indium and titanium are superconducting. For AEgIS only the normal conducting case matters, since the experiment will operate in an 1 T magnetic field background. For a better understanding of the heat transport processes in the samples, the thermal diffusivity in superconducting and normal conducting state is measured.

4. Investigation of the measurement method

The AC measurement method described in section 2.4.2 was already used by C. van der Post in [10] and T. Eisel et al. [37] to study the thermal diffusivity of the sapphire-indium-copper sandwich at ultra-low temperatures. The results of the different studies did not give explicit conclusions. A frequency dependence was observed by using the phase shift and the amplitude damping to calculate the thermal diffusivity of the sandwich. Furthermore, the absolute values for the thermal diffusivity were smaller than expected from literature. First steps to analyze the measurement method have already been undertaken by C. van der Post. He measured the thermal diffusivity of copper, a well known material, at ultra-low temperatures with the same set-up as used for this work. C. van der Post used the phase shift between the heater and the temperature sensor on the stamp itself, see Figure 3.4, to calculate the thermal diffusivity of copper at about 100 mK. The measured thermal diffusivity values were five orders of magnitude below the literature value. The results raise the question, weather the AC method can be used for the described experimental set-up. To validate the method and to exclude faults in the experimental set-up, the measurement chain is analyzed and further experiments are performed on a well known reference sample.

4.1. Measurement chain and phase shift method accuracy at ultra-low temperatures

At first the measurement chain of the set-up in the dilution refrigerator was checked and the reproducibility of the measured results was studied to define an accuracy of the method. For the temperature measurements at ultra-low temperatures two types of Ruthenium Oxide sensors (RX-Sensors: R (30 mK) $\approx$ 80 kΩ and R (300 mK) $\approx$ 4 kΩ; T-Sensors: R (30 mK) $\approx$ 8 kΩ and R (300 mK) $\approx$ 2.5 kΩ) were used [10].

The ultra-low temperature measurements make additional devices in the measurement chain necessary, such as an AC resistance bridge. For a sensor used in the milliKelvin range it is required to avoid excessive self-heating. At room temperature self-heating of about 10 mK can be neglected but in the milliKelvin range it means a considerable measurement error. Consequently, extremely low measurement currents have to be used, that are too low to be generated by ordinary ohmmeters. The low currents can be achieved with cryogenic resistance bridges. The voltage drop is extremely small at such low currents and it may vanish in thermal and contact voltages or offset voltages of the instrument. All cryogenic resistance bridges use AC lock-in amplifier to block the thermal and offset voltages. Furthermore, the instrument is specially designed for a low-noise input stage and in addition to many resistance ranges, different currents can be used for each resistance range. That enables to choose the best trade-off between signal-to-noise ratio and self-heating error [39]. Consequently, it is not possible to forego the resistance bridge for the measurements in the milliKelvin range. The disadvantage is that the device might cause an additional phase shift and could be the reason for the false thermal diffusivity values obtained. Based on the high temperature gradient between stamp and platform ($T_{Stamp} \gg T_{Platform}$) both sensors operate in different ranges of the AC resistance bridge (ΔR $\approx$ 5...50 kΩ).
Measurements at room temperature are performed, investigating the measurement chain shown in Figure 4.1, to determine the accuracy of the phase shift method (1) and to identify additional phase shifts (2) & (3).

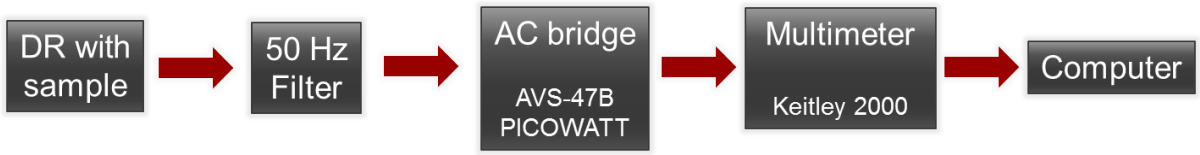

Figure 4.1: Schematics of the measurement chain at ultra-low temperatures.

For the studies a heater and a temperature sensor were glued directly together and connected to the measurement chain replacing the "DR with sample" in Figure 4.1. The mock-up is accommodated at room temperature and was heated with different powers in order to reach different temperature ranges. To replace the Ruthenium Oxide sensor a thermistor was chosen. The thermistor reaches similar ΔR with the described mock-up as the Ruthenium Oxide sensors at ultra-low temperatures and reacts fast enough. With this set-up different ranges of the AC resistance bridge were checked and the influence of the bridge in general was verified.
The measurement chain should not influence the amplitude measurements. Therefore, the amplitude method is studied separately for possible errors in section 4.2.

(1) Reproducibility of the measurement including fit

First, the accuracy of the phase shift method performed with the used set-up is determined. Therefore, the described thermistor and heater are used. A function generator applies a sinusoidal heat signal with the typical frequencies (f= 1/15 Hz, 1/30 Hz, 1/60 Hz) used for measurements already performed cf. [1, 10] and also higher frequencies (f = 0.1 Hz and 0.2 Hz). Several measurements are performed for each frequency. The measurement data is plotted, fitted and the phase shift is determined. The accuracy at the different frequencies is listed below. The measurements are performed in the 20 kΩ and the 200 kΩ range of the AC resistance bridge, typical ranges used for the sandwich measurements at ultra-low temperatures later on. The accuracy is similar for the two ranges tested. To calculate the thermal diffusivity the phase shift in radian is needed, see (27). Therefore, the following equation is used to determine the phase shift in radian, where $T_{per} = 1/\mathrm{f}$:

$$\varphi(rad) = \frac{\Delta t(s) * 2\pi}{T_{per}} \quad . \tag{28}$$

Table 1 shows that the measurement accuracy in radian decreases when using a high measurement frequency of 0.2 Hz. Consequently, measurements using the phase shift to calculate the thermal diffusivity are more accurate at low frequencies.

Table 1: Sensor accuracy of a phase shift measurement.

Frequency (Hz)	Accuracy (s)	Accuracy (rad)
1/60	± 0.41	± 0.05
1/30	± 0.15	± 0.03
1/15	± 0.08	± 0.04
0.1	± 0.03	± 0.04
0.2	± 0.08	± 0.21

(2) Thermal diffusivity determined from the phase shift between two sensors signals

The comparison of two temperature sensors is used at ultra-low temperatures to gain information about the thermal diffusivity of the sandwich. Both sensor signals have to pass the measurement chain illustrated in Figure 4.1. It is of importance to mention, that the signals of the sensors can not be measured at the same time and are often measured in different ranges of the AC resistance bridge. They are measured successively and later the timing of the heater signal is used to merge them. A different phase shift between the two sensor signals caused by a measurement in different AC bridge ranges might occur and can lead to errors in thermal diffusivity measurements.
The ranges 20 kΩ and 200 kΩ are studied here. To reach the 200 kΩ range an additional

resistance was added in the circuit of the thermistor, the heater and the thermistor were not changed. The same measurements are performed in both ranges, aligned with the heater signal and the phase shift between the ranges was determined.
Figure 4.2 (left) shows the measured phase shift in seconds and radian between the measurements performed in the 20 kΩ and 200 kΩ range. The measurement in the higher range reacts always first and the lower range has a delay. The phase shift in radian increases with frequency and amounts to ~ 0.3 rad at 0.2 Hz. Comparing these phase shifts in radian with the determined measurement accuracy in Table 1, one sees that the phase shift caused by the different ranges is smaller than the measurement accuracy for almost all frequencies (except 0.1 Hz). That means that error caused by the different ranges can be neglected.

(3) Thermal diffusivity determined from the phase shift between heater and sensor

Measurements performed at ultra-low temperatures comparing the phase shift between heater and temperature sensor gave much too low thermal diffusivity values for copper [10]. The sensor signal coming from the dilution refrigerator (DR) passes a 50 Hz filter, an AC resistance bridge and is then saved in the internal buffer of a Keithley digital multimeter and afterwards forwarded to a computer. The heater signal does not pass through the whole measurement chain, it does not have to pass through the AC resistance bridge. To check for an additional phase shift caused by the AC resistance bridge the device was removed from the chain. The same measurements with and without the AC bridge were performed and later merged in time with the heater reference signal. The results can be found in Figure 4.2 (right). The phase shift caused by the resistance bridge is

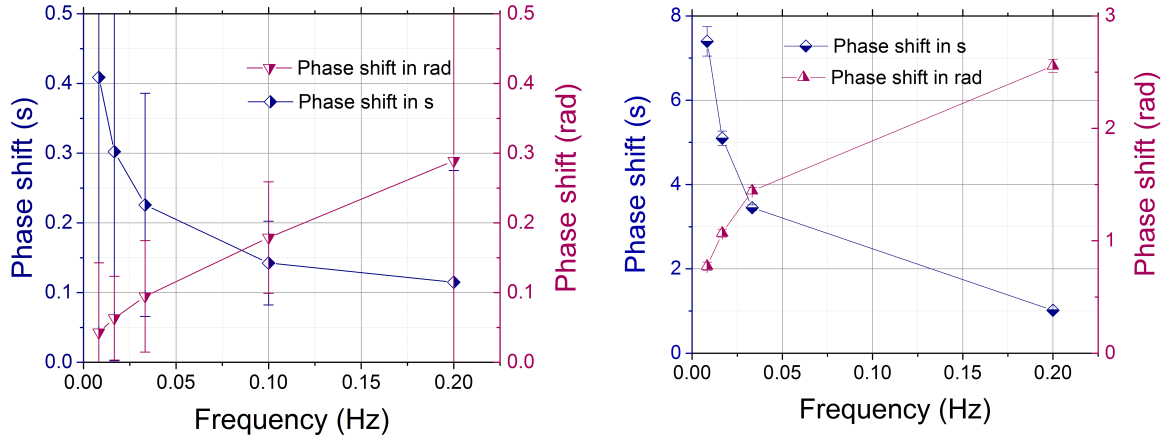

Figure 4.2: Phase shift between signals measured in the 20 kΩ and the 200 kΩ range (left) and between signal measured with and without resistance bridge (right).

at low frequencies higher than 7 seconds. That strong effect on the measurement cannot be neglected and thus the comparison between a heater signal and temperature sensor

signal cannot be used to determine the thermal diffusivity with the phase shift method. The results also explain the five orders of magnitude smaller thermal diffusivity values obtained for copper at ultra low temperature by C. van der Post [10].
The conclusions of checking the measurement chain are that a comparison between a heater signal and a temperature sensor signal cannot be used to determine the thermal diffusivity. The comparison of two sensor signals can be used within the determined accuracy. For the studied sandwich the method can be excluded. The sandwich has a high thermal diffusivity and at low temperatures it would lead to a small phase shift value within the range of the accuracy of the set-up. The method is only valuable for thermal diffusivity measurements on samples with low thermal diffusivity. For that reason no further experiments at ultra-low temperatures using the phase shift method will be performed.

4.2. Measurements on a reference sample

The reference sample consists of oxygen-free high conductivity copper (OFHC), since it is a well characterized material. The AC method was first studied at room temperature and at liquid nitrogen temperature (T $\sim$ 77.5 K). To minimize heat convection between the sample and the surrounding, the copper bar was placed in a vacuum chamber (p $< 10^{-4}$ mbar) and attached to the vacuum chamber lid as a heat sink cooled at the outside by water or liquid nitrogen. The sample cross section the heat flows through is 8.4 mm x 8.4 mm. A heater was glued on the top side of the sample, shown in Figure 4.3.

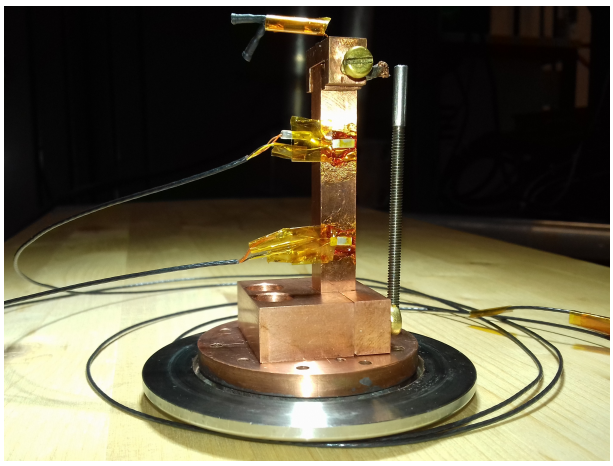

Figure 4.3: Copper reference sample on the vacuum chamber lid.

For the temperature measurements Pt100 resistance sensors were used. The first sensor Pt100.1 was attached at a distance of 1.53 cm from the heater and the second Pt100.2 at a distance of 3.65 cm, both by indium cold welding. The distance between the two sensors amounts to 2.12 cm. Figure 4.3 shows the copper sample attached to the vacuum chamber lid prepared for measurements at room and liquid nitrogen temperatures. For

the measurements the vacuum chamber was placed either in a water tank or in a liquid nitrogen dewar.

The AC method was explained in section 2.4.2. As mentioned in section 3.3, measurements on the sandwich at ultra-low temperatures were already performed and showed a dependence of the thermal diffusivity on the frequency of the applied heat signal. For the measurement on the reference sample the same frequencies as used for the sandwich (f = 1/15 Hz, 1/30 Hz, 1/60 Hz) are studied. Additionally, higher and lower frequencies are investigated to give a better overview of the frequency dependence.

A typical measurement curve of our investigations is shown in Figure 4.4 (left) with a frequency of 0.2 Hz. The curve on the top shows the signal, which was closer to the heat source. The attenuated curve is illustrated below. For these two curves the amplitude ratio is determined and the thermal diffusivity calculated with equation (27).

The thermal diffusivity calculated for the different frequencies is shown in Figure 4.4 (right) for liquid nitrogen and room temperature. One can see a frequency dependence at low frequencies for the thermal diffusivity, as already reported for the sandwich measurements at ultra low temperatures [10]. At higher frequencies the curve flattens and a constant thermal diffusivity can be deduced. The threshold frequency f_c, where the thermal diffusivity flattens, is temperature dependent. At T $\sim$ 297 K $f_c \sim$ 0.06 Hz and at T $\sim$ 77 K $f_c \sim$ 0.20 Hz. The constant values for the thermal diffusivity are $D_{297K} = 1.2 \pm 0.2$ cm^2/s and $D_{77K} = 3.2 \pm 0.3$ cm^2/s. The corresponding literature values are $D_{300K} = 1.15$ cm^2/s and $D_{80K} = 3.1$ cm^2/s [40]. The measured values show good agreement with literature data. The measurement error increases with frequency because of the decreasing amplitudes. It follows that the AC amplitude method can be used for

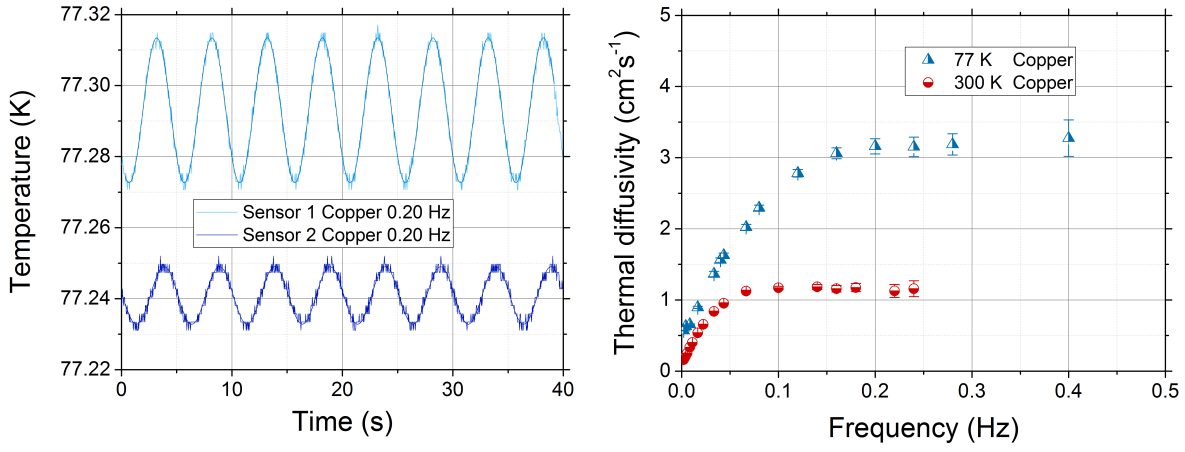

Figure 4.4: Sinusoidal heat signal f = 0.2 Hz on copper (left) and thermal diffusivity versus frequency for copper at 77 K and 300 K (right).

frequencies higher than f_c at room temperature down to liquid nitrogen temperatures. Since the measurements performed on the sandwiches are in the milliKelvin range, it is important to gain more information about the temperature dependence and threshold

frequency of the AC amplitude method. It is not possible to measure the reference sample at ultra-low temperatures without significant effort. Therefore, the test sample was studied at low temperatures using the cryocooler set-up introduced in section 3.1 .
The sample was mounted on a cryocooler and measurements between 25 K and 55 K were performed. The increasing threshold frequency limits the measurements at low temperatures. The signal to noise ratio became too small and it was difficult to identify the amplitude of the temperature oscillation. This is why the signal was fragmented in its frequency components by a fast Fourier transformation (FFT). The FFT was performed using a MATLAB function. The pure signal at T $\sim$ 49 K and for a measurement frequency of f = 0.8 Hz is illustrated in Figure 4.5 (left). The amplitude of the temperature signal versus the frequency is shown in the graph on the right. Here, the signal amplitude at the given frequency can be easily identified.

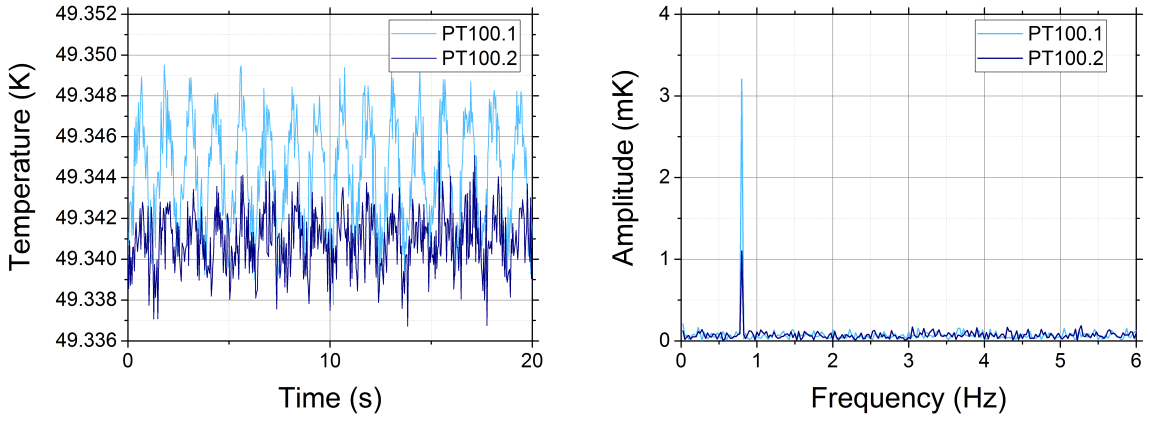

Figure 4.5: Sinusoidal heat signal f = 0.8 Hz on copper (left) and amplitude versus frequency at about 49 K (right).

The measurement is performed down to 25 K and an increase in thermal diffusivity is observed like expected from literature. At low temperatures the signal was very noisy and the threshold frequency was too high to measure the plateau. Therefore, an exponential fit curve was used to identify the value of the thermal diffusivity in the constant part at higher frequencies, where a measurement was not possible. For the measured constant parts of the thermal diffusivity at different temperatures the standard deviation was $\sim$ 20 % of the absolute value. This was taken as the error for the thermal diffusivity, knowing that the error can be larger at low temperatures, where the threshold frequency was not reached with the measurement. The data points for the thermal diffusivity obtained by analyzing the measured data from the cryocooler with a FFT for different temperatures and frequencies including the exponential fit of the data are shown in Figure 4.6 for temperatures between 25 K and 56 K. Additionally, the threshold frequency f_{c1} is studied. Therefore, the frequency at which 90 % and 100 % of the final thermal diffusivity

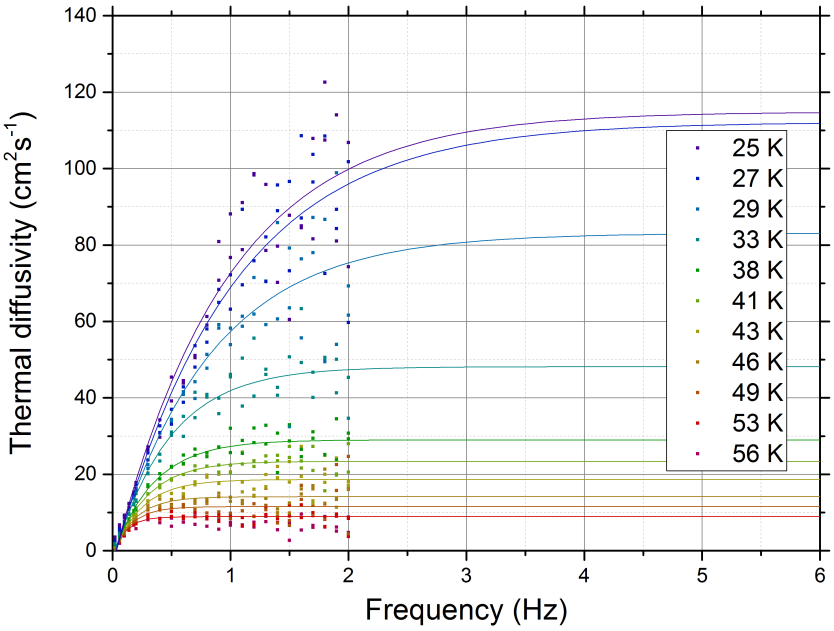

Figure 4.6: Thermal diffusivity of copper versus frequency including exponential fit for the cryocooler measurements (temperature decreases from bottom curve to top curve).

is first reached was plotted versus the temperature. The graph 4.7 shows the estimation of the threshold frequency over the whole temperature range between 25 K and 300 K. It is noticeable that there is a change in the slope of the curve between 56 K and 77 K.

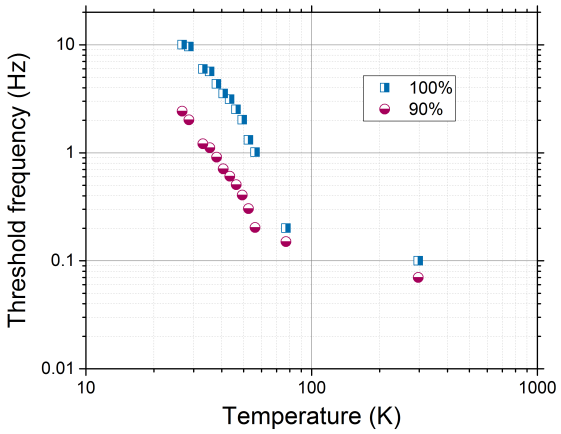

Figure 4.7: Threshold frequency for copper versus temperature.

The measurements at 77 K and 300 K are performed in a vacuum chamber immersed in water or liquid nitrogen. The measurements below 77 K are performed with a cryocooler. The change might indicate that the threshold frequency is influenced by the measurement system and, thus, is a system specific parameter. Furthermore, the threshold frequency seems to be also related to the thermal diffusivity value of the sample material at least

for the same measurement apparatus. A decrease of the thermal diffusivity also results in a decrease of f_{c1}. Consequently, it is easier to measure materials with a low thermal diffusivity, because the plateau can be reached already at low frequencies.
The values of the thermal diffusivity versus temperature measured with the described set-ups are shown in Figure 4.8 and illustrated in blue. The red line shows literature values of the thermal diffusivity of copper [40]. There is a good agreement between the measured values and the values from literature which were calculated below 150 K. At lower temperatures a slight difference of the measured thermal diffusivity values compared to literature data occurs. As mentioned above the threshold frequency at low temperatures was very high, what made it hard to detect the constant part of the curve below 40 K and may cause additional errors. The difference in thermal diffusivity between measurement and literature data can be explained by a difference in residual-resistivity ratio (RRR) which is a measure of the purity of a material. The measurement sample consists of OFHC (99.99 % copper, RRR minimum 50, λ (4 K) minimum 400 W/(m·K) [41]) but after machining the sample no heat treatment has been performed which may have influenced these values. The literature data is for copper with higher purity (99.999 % copper, annealed) which results in higher thermal diffusivity values at low temperatures. That difference in purity is visible in the graph and shows again the good agreement between literature values and measured values. From this results can be concluded that the amplitude method is suitable for the sandwich measurements.

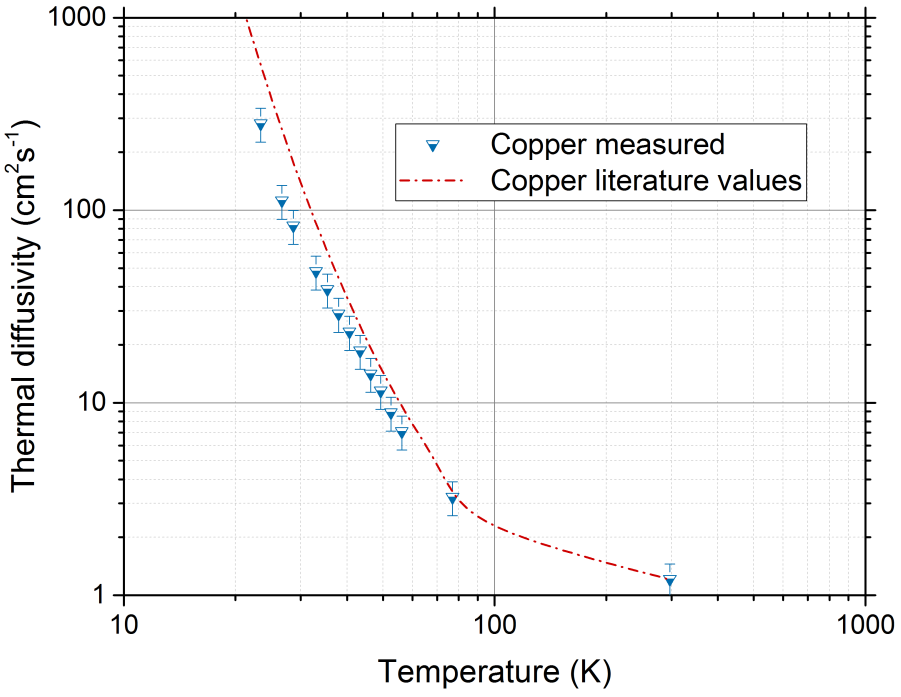

Figure 4.8: Thermal diffusivity of copper sample between 30 K to 300 K from measurement and literature values [40].

5. Thermal diffusivity measurements on the sandwich

5.1. Measurements at low temperatures

For the thermal diffusivity studies of both sandwich designs in the temperature range from 3 K to 30 K the 2-stage pulse-tube refrigerator, described in section 3.1, is used. The damper for thermal oscillations explained in the same section is only used for studies of the sapphire-indium-gold-titanium-copper sandwich. It was just made available for this measurement run. The amplitude damping of the AC method is used to determine the thermal diffusivity, since the reference sample measurements using this method yielded the best results in accordance to literature values. The mock-up for the thermal diffusivity studies of the different sandwich types mounted at the CERN Cryolab pulse-tube refrigerator is shown in Figure 5.1. The picture shows the sapphire-indium-gold-titanium-copper sandwich mock-up. The platform design for the sapphire-indium-copper sandwich (S1) and sapphire-indium-gold-titanium-copper sandwich (S2) differ by an additional copper block for S2. The platform without the copper block for S1 can be found in the appendix, see Figure A.3. Based on the additional copper block the distance between the temperature sensors is different for S1 ($d = 1.975$ cm) and S2 ($d = 2.775$ cm). Both mock-ups are mounted upside down on the experimental platform. The heater on the 2nd stage (HT2) of the refrigerator is used to change the base temperature of the experimental platform.

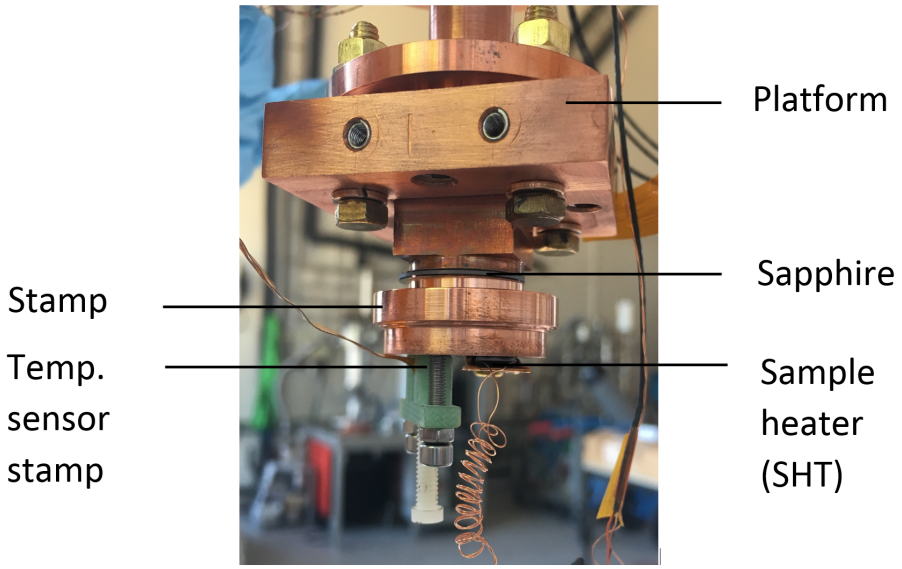

Figure 5.1: Sandwich design S2 mounted on the pulse-tube refrigerator. The cold welded indium ensures mechanical support in the upside down mounting orientation.

Cernox temperature sensors are used for the measurements. One is clamped to the top of the copper stamp and the other one is attached to the side of the copper platform by a clamping structure bolted through holes in the platform (not shown in the picture). For better thermal contact an indium foil is added in between the temperature sensors and

the copper. The sample heater (SHT) is glued to the stamp and a function generator is used to supply a sinusoidal heat signal. Sample heater peak-to-peak voltages between 4 V and 20 V are used for the studies. The different heating powers cause different temperature gradients in the sandwich. For each SHT voltage at each base temperature frequencies between 0.02 Hz up to 10 Hz or 12 Hz are measured and the thermal diffusivity is determined.

5.1.1. Results

The thermal diffusivity versus the frequency for the sapphire-indium-copper sandwich mock-up is shown in Figure 5.2. From the frequency dependence studies of the refer-

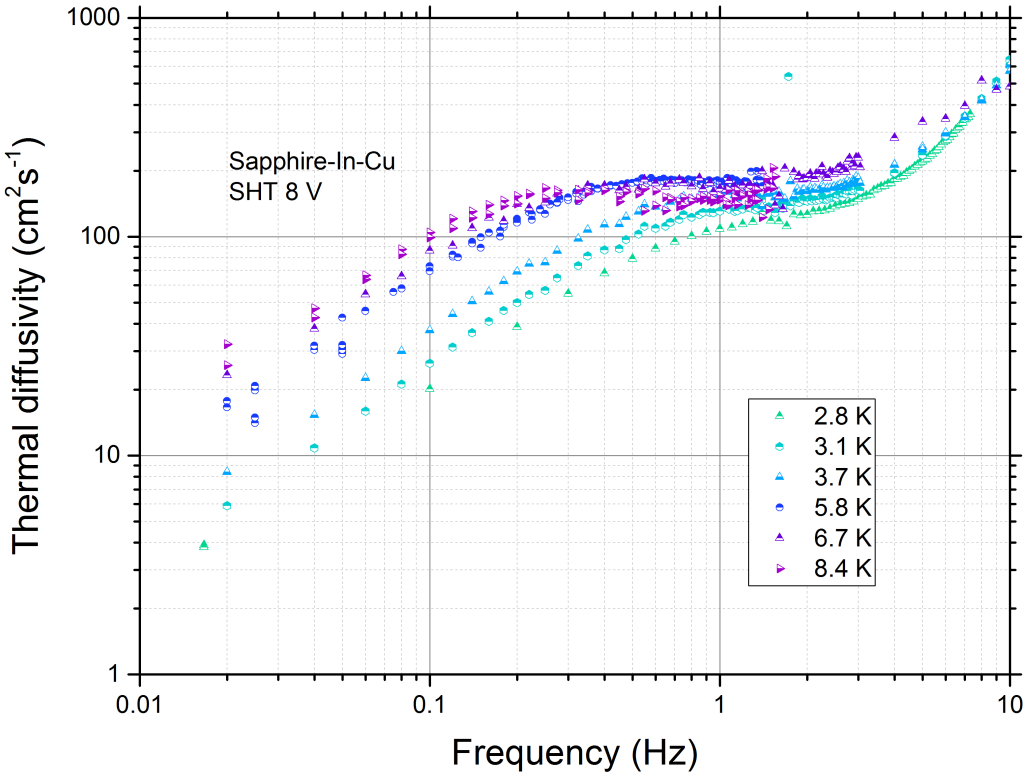

Figure 5.2: Frequency dependence of the thermal diffusivity for S1. The sample heater (SHT) was supplied with an 8 V AC signal from the function generator.

ence sample, an increase of the thermal diffusivity until it reaches a constant plateau is expected. A similar behavior was found for the sapphire-indium-copper sandwich. The thermal diffusivity increases with frequency until it reaches constant values. The threshold frequency for the plateau is temperature dependent. The measurement is performed without the damper described in section 3.1. For the measurements without damper, a resonance peak of the thermal diffusivity can be found at about 1.7 Hz (only shown for T = 3.1 K in Figure 5.2), the frequency of the pulse-tube cryocooler temperature oscillations. In addition to the first threshold frequency one sees in Figure 5.2 that the thermal

diffusivity starts to increase again after the plateau for frequencies approaching 10 Hz. The second threshold frequency seems to be also temperature dependent. The graph shows only a few representative plots at low temperatures. Many more measurements performed at higher base temperatures showed the increase of thermal diffusivity after the plateau as well. It is not clear if the same behavior would also appear for the copper reference sample at higher frequencies, which was only measured up to 2 Hz. Results at higher frequencies using the PT100 temperatures sensors are too noisy for calculations of the thermal diffusivity. It could indicate another influence caused by the experimental set-up (heater supply, cabling).

To define the final thermal diffusivity at a certain temperature, the plateau was chosen to give the characteristic value for the sandwich. The function was exponentially fitted below the second threshold frequency. The corresponding temperature for each plateau is the mean temperature between the mean stamp and mean platform temperature. Error propagation gives a different error for each point on the plateau increasing with frequency, as seen already in section 4.2. Hence, the error bar of the final frequency independent thermal diffusivity at the plateau is taken from the standard deviation of the thermal diffusivity between 1 Hz and 2 Hz, the area of the plateau.

Figure 5.3 shows the frequency dependence of the thermal diffusivity for the sapphire-titanium-gold-indium-copper sandwich for a sample heater voltage of 20 V without the use of the damper. The measurement points showing strong resonances around 1.7 Hz are not plotted here. The curve shape is the same as seen for the sapphire-indium-copper sandwich. Figure 5.4 shows the same measurement, but for different base temperatures and using the damper to avoid the resonances at 1.7 Hz. It is remarkable how much the use of the damper changes the shape of the thermal diffusivity curves at low frequencies. Basically, one gets much higher thermal diffusivity values at low frequencies by using the damper than without the damper and thus the first threshold frequency changes. It was already presumed in section 4.2 that the first threshold frequency could be dependent on the measurement set-up. Here, one sees clearly that a change of the system, by adding a high heat capacity material between cold head and experimental platform, strongly influences the first threshold frequency but the plateau values are similar. At temperatures below 7.3 K the thermal diffusivity values below the first threshold frequency are even higher than the plateau values. The influence of the damper becomes even more obvious for the measurements using 8 V SHT, see Figure A.4 and Figure A.5. At temperatures of about 4.4 K the value at low frequencies is between 150...250 cm^2/s and at the plateau not much higher than 100 cm^2/s.

These results make it difficult to judge which value to take for the final thermal diffusivity at a specific temperature. It was decided to take the plateau to define the thermal diffusivity dependency from temperature although the thermal diffusivity is higher below and above the plateau for some measurement series. For higher temperatures it is very

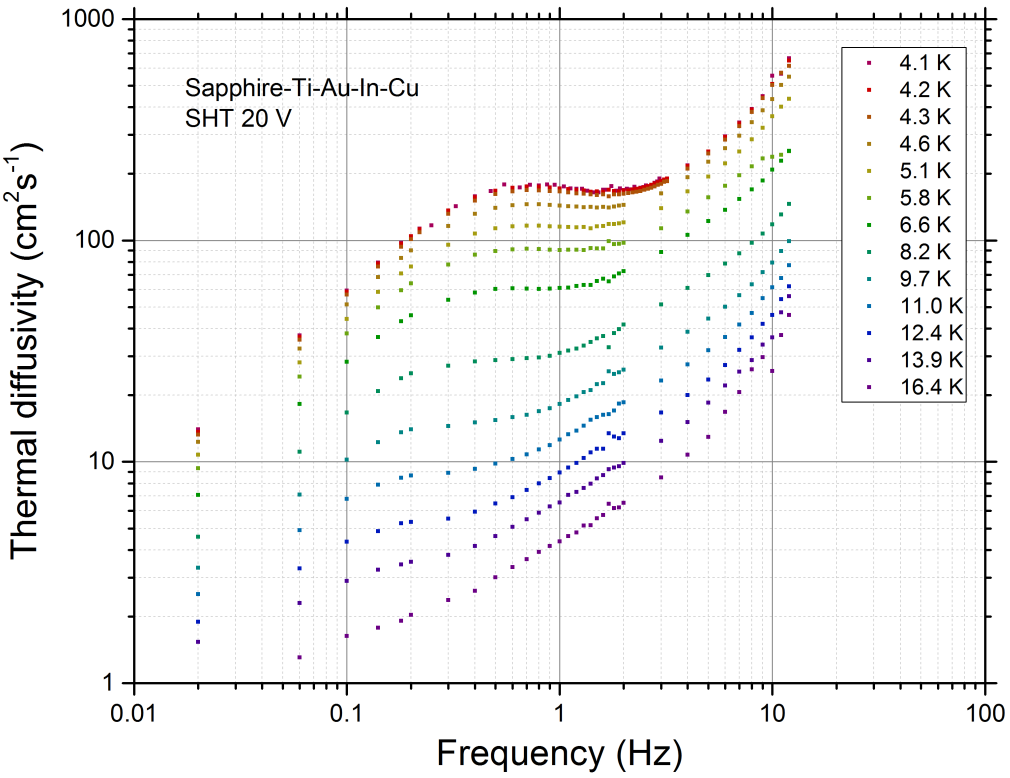

Figure 5.3: $D_s(f)$ for S2 measured without the damper for SHT 20 V (temperature decreases from bottom curve to top curve).

difficult to define a plateau in the graphs, since the thermal diffusivity seems to increases with a constant slope. Thus, the results between 10 K and 30 K are not very precise.
The temperature dependence obtained by fitting the plateau of thermal diffusivity is shown for both sandwich mock-ups in Figure 5.5. The figure shows the results of several measurement runs at different base temperatures. Furthermore, it shows different measurement runs with SHT peak-to-peak voltages applied with the function generator of 4 V, 8 V, 10 V and 16 V for the sapphire-indium-copper sandwich and 4 V, 8 V and 20 V for the sapphire-titanium-gold-indium-copper sandwich. Additionally, results with and without the use of the damper for the sapphire-titanium-gold-indium-copper sandwich are plotted.
One sees a good overlap of the resulting thermal diffusivity values obtained at the plateau with and without using the damper. Data of high SHT peak-to-peak voltages such as 16 V or 20 V deviate from the results obtained with lower sample heater voltages between 3 K and 5 K for both sandwiches. The deviating results are obtained without the damper. The difference may be caused by the increased temperature gradient over the sandwich. The temperature used for each data point is, as mentioned before, the mean value between the stamp and platform temperatures. The resulting mean temperature for a higher heat load might be the same as for the smaller heat load, but platform and stamp

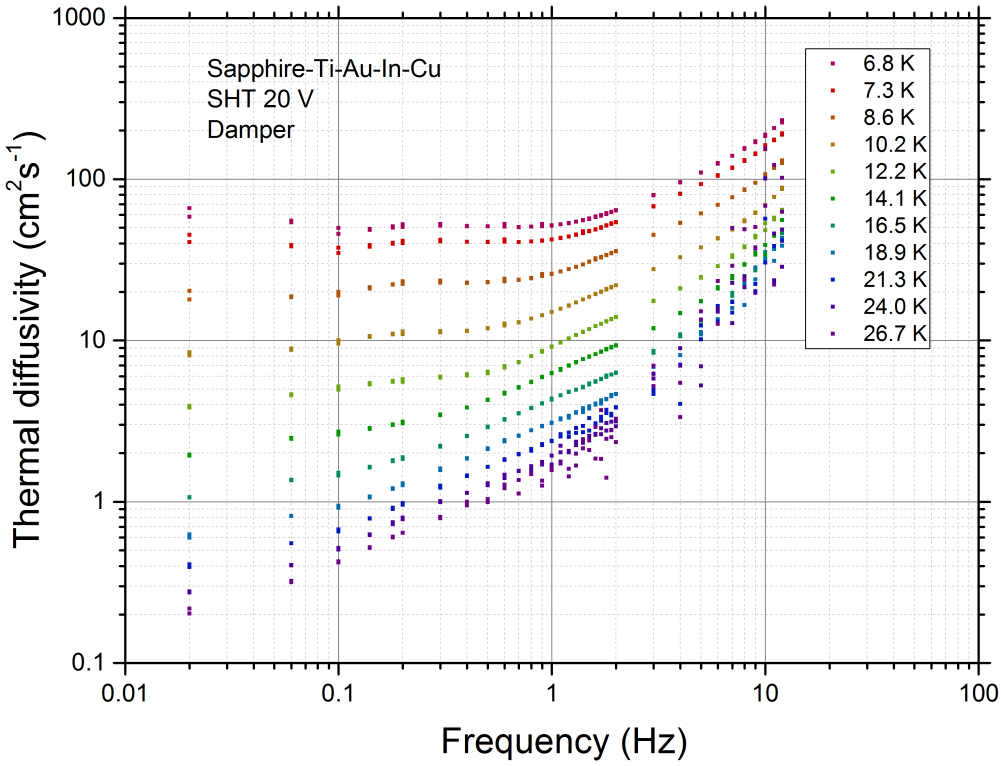

Figure 5.4: $D_s(f)$ for S2 measured with the damper for SHT 20 V (temperature decreases from bottom curve to top curve).

are at different temperatures. These differences in temperature gradient might cause the mismatch in thermal diffusivity for the high SHT voltages. The influence vanishes at high temperatures, where the change in temperature gradient is smaller in comparison to the absolute temperature. All the other results measured with different SHT voltages (4 V, 8 V and 10 V) applied overlap at the same mean temperature. Furthermore, the results obtained with and without the damper are the same for low SHT voltages (4 V, 8 V).
The thermal diffusivity of both sandwiches has a peak and decreases with higher temperatures as expected from theory. The peak is at about 6 K for the sapphire-indium-copper sandwich (S1) and at about 4 K for the sapphire-titanium-gold-indium-copper sandwich (S2). The thermal diffusivity for S2 is smaller than for S1 at high temperatures and both curves merge at about 3 K. The merge at low temperatures does not match our expectations of a smaller thermal diffusivity for the S2 sample compared to the S1 sample. It was assumed that the increase in thermal boundary resistance leads to an decrease of the thermal diffusivity of the sapphire-gold-titanium-indium-copper sandwich. Regarding this theory it is surprising that the two graphs seem to merge at temperatures T below the peak temperature T_{peak}. The influence of thermal boundary resistance increases at low temperatures. Consequently, it was expected that the curves would overlap at high temperature and split more and more at low temperatures.

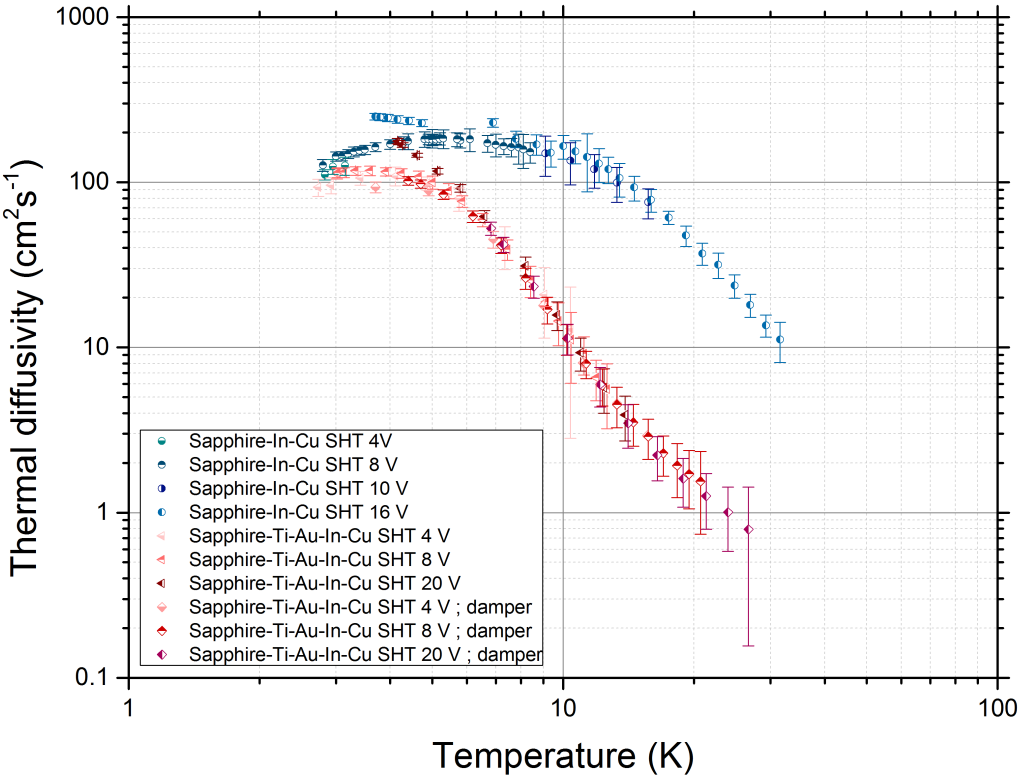

Figure 5.5: Thermal diffusivity at low temperatures for both sandwich samples with different supplied heat load excitations at the stamp. Thermal diffusivity values are taken at the plateau of the frequency dependence curves.

5.1.2. Modeling

To check weather the values obtained for the thermal diffusivity at the plateau are realistic or not, the sandwich thermal diffusivity was modeled with literature values for the single elements of the sandwich. The thermal diffusivity is defined as thermal conductivity divided by the heat capacity and density, as seen in equation (18). To minimize errors in the modeling, a combination of measurement and modeling is chosen:

$$D_{modeled} = \frac{\lambda_s^{measured}}{c_s^{modeled} \cdot \rho_s^{modeled}} \quad . \tag{29}$$

The thermal conductivity values can be measured directly with the described set-up and can be used as input for the model. A steady state method is used. By heating the sample with a constant power the steady state temperature gradient across the sandwich can be measured. It is important to wait until both temperatures are constant before defining the gradient [34]. By using equation (8), the thermal conductivity can be calculated for the sample using the measured gradient. A typical steady state measurement curve is illustrated in the appendix, see Figure A.2. The measurement results for both sandwich designs are illustrated in Figure 5.6, the error bars are in the range of the point size. As expected due to the thermal diffusivity measurements, the thermal conductivity of

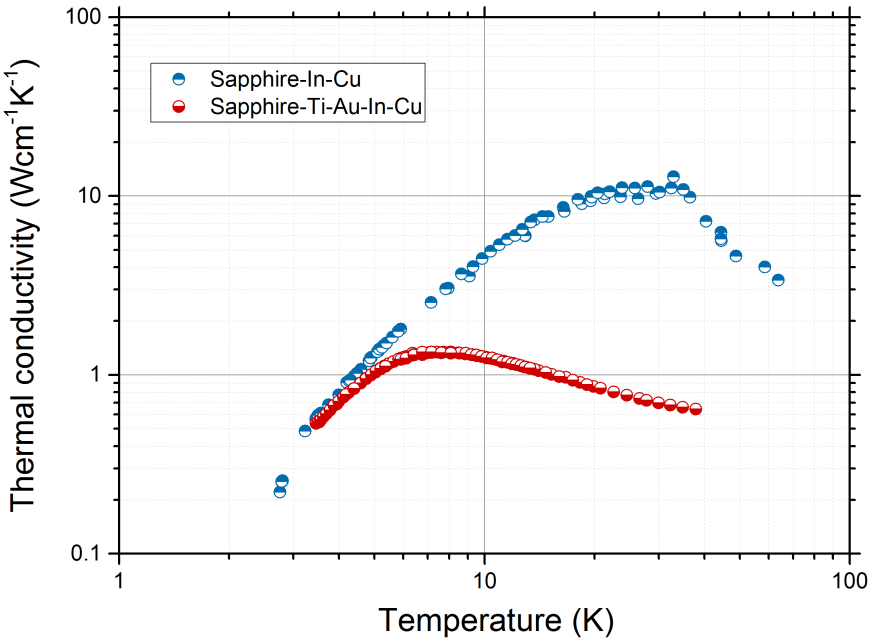

Figure 5.6: Thermal conductivity of both sandwiches S1 and S2 at low temperatures. Measurements are performed using a steady state method described in [34].

the sapphire-titanium-gold-indium-copper sandwich is smaller than that of the sapphire-indium-copper sandwich at high temperatures. The peak for S1 is at about 30 K and the value is almost one order of magnitude higher than for S2. The maximum in thermal conductivity for S2 is moved to lower temperatures and is at about 7 K. At temperatures below 4 K both curves merge as seen already at the thermal diffusivity measurements.
The measured thermal conductivity for the sapphire-indium-copper sandwich was modeled. The modeling of the thermal conductivity of a sandwich mock-up is necessary in order to gain information about the distances measured and to see the influence of the thermal boundary resistance. Furthermore, the sandwich mock-up does not have a constant cross section over the whole distance. It needs to be checked if considering the minimum cross section leads to reliable results in modeling. To model the final thermal conductivity, the thermal resistances of each material taken from literature values are added up in series like shown in equation (19). The thermal conductivity was calculated from the thermal resistance using equation (20), while applying the minimum cross section of the sandwich and considering the total distance between the center of the temperatures sensors to be 1.975 cm. The results of the modeling are shown in Figure 5.7. The discontinuous lines illustrate the literature values for copper [40], indium [40] and sapphire [42]. The measured values for the sandwich including error bars are plotted in a diamond shape. The continuous lines are the modeled values. The first line with the highest thermal conductivity at 4 K is modeled without the boundary resistance (a). The line below is modeled including the boundary resistance values taken from [23] and a temperature

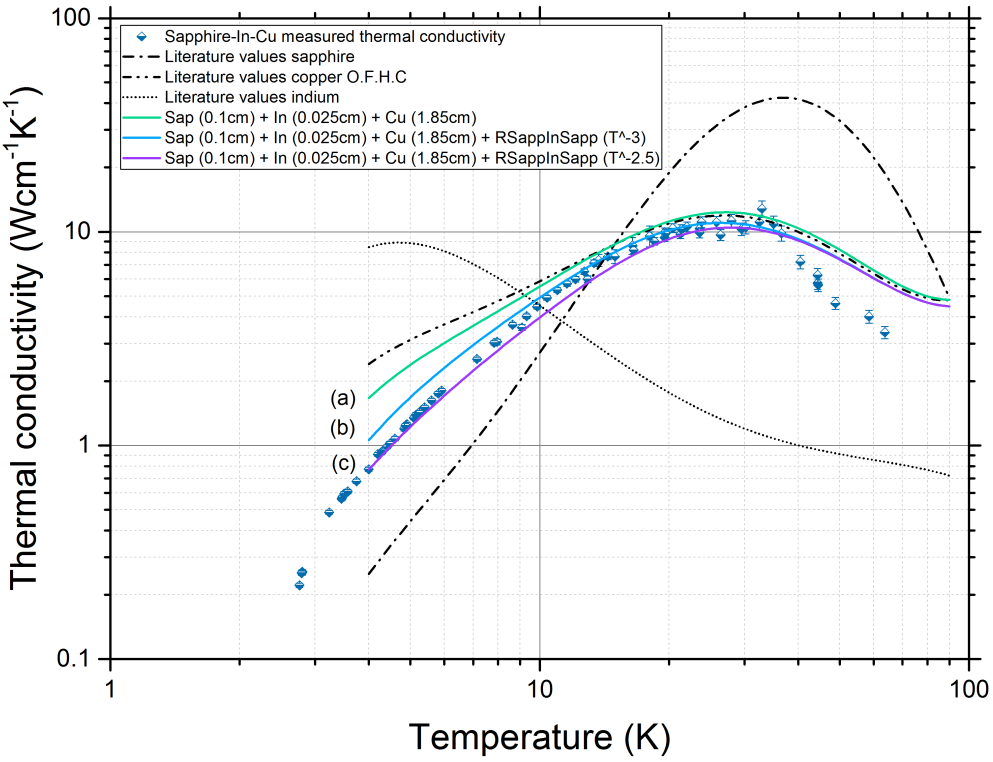

Figure 5.7: Comparison of measurement results and modeling of the thermal conductivity for S1: Modeling (a) without thermal boundary resistance, (b) including thermal boundary resistance (T^{-3} dependence), (c) including thermal boundary resistance ($T^{-2.5}$ dependence).

dependence of T^{-3} as suggested from theory (b). At ultra-low temperatures J. Liberadzka measured a temperature dependence of the thermal boundary resistance for the same sandwich to be below T^{-3}. A model, assuming a $T^{-2.5}$ dependence of the thermal boundary resistance (c), delivers results overlapping well with the measured values for the sandwich at low temperatures and gives the lowest thermal conductivity of the three models. Taking the thermal boundary resistance into account influences the modeling of the thermal conductivity only at temperatures below the maximum in thermal conductivity. Afterwards the influence vanishes. At temperatures above 35 K the values from the modeling and the measurement differ. The reason might be an inaccurate measurement. At higher temperatures it takes a long time until steady state conditions are reached in the measurement process. The thermal conductivity was calculated when the temperature was still slightly increasing. That might have caused measurement errors. It is also possible that an effect occurring at $T > T_{\lambda_{max}}$ is not included in the model. Only data below 30 K is of importance for the thermal diffusivity modeling, thus, the discrepancy at higher temperatures can be neglected. The combination of the materials in series are reproducing well the maximum peak and the low temperature behavior of the thermal

conductivity.
How to add up the heat capacity times the density is described in equation (21). The given equation is for a constant cross section. For the sandwich mock-up the cross section changes. The calculation of $c_s \cdot \rho_s$ was done, assuming a constant cross section and also considering the real volumes of each material described by:

$$c_s \cdot \rho_s = \sum_i \frac{V_i}{V_{total}} \cdot c_i \cdot \rho_i \quad . \tag{30}$$

The results using equation (21) or (30) are almost identical. Afterwards, the measured thermal conductivity for each sandwich was divided by the modeled total heat capacity times the density following equation (29). The results of the modeling are shown in Figure 5.8 and Figure 5.9 and compared with the measurement. The sapphire-titanium-gold-indium-copper sandwich was modeled without the heat capacity of the titanium layer, since it has almost no influence to the heat capacity because of the small thickness of 50 µm. Literature values for the heat capacity of gold [43], indium [17] and copper [40] are used for the model. The modeling of thermal diffusivity shows a difference compared to the measured values. For both sandwiches the curve shape is similar for measurement and modeling, even the maxima occur at the same temperature, but the absolute values differ.

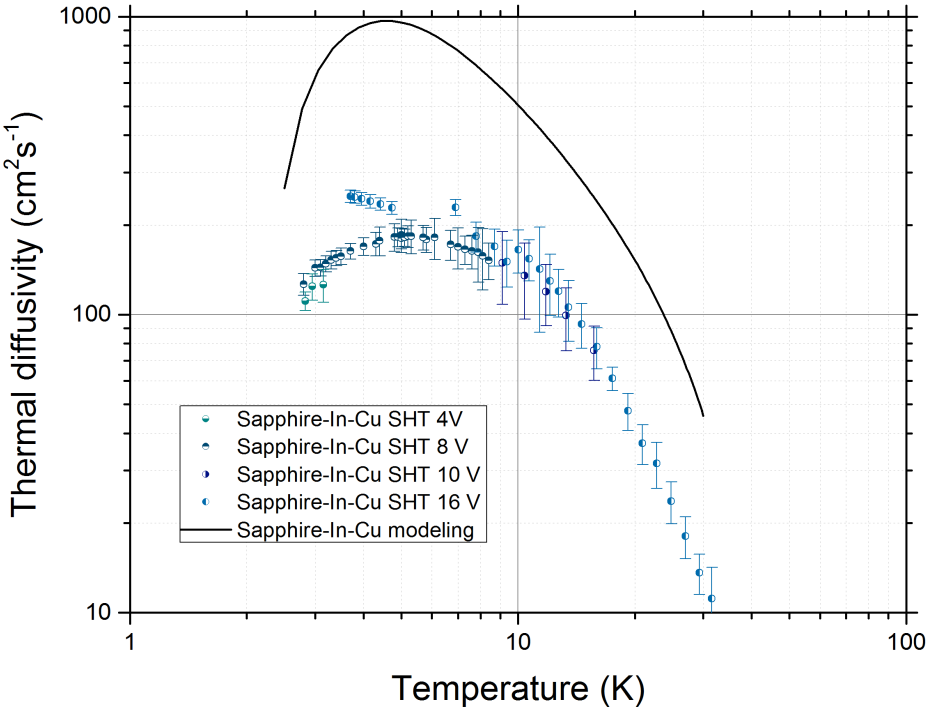

Figure 5.8: Comparison between measured and modeled values for $D_s(T)$ of S1.

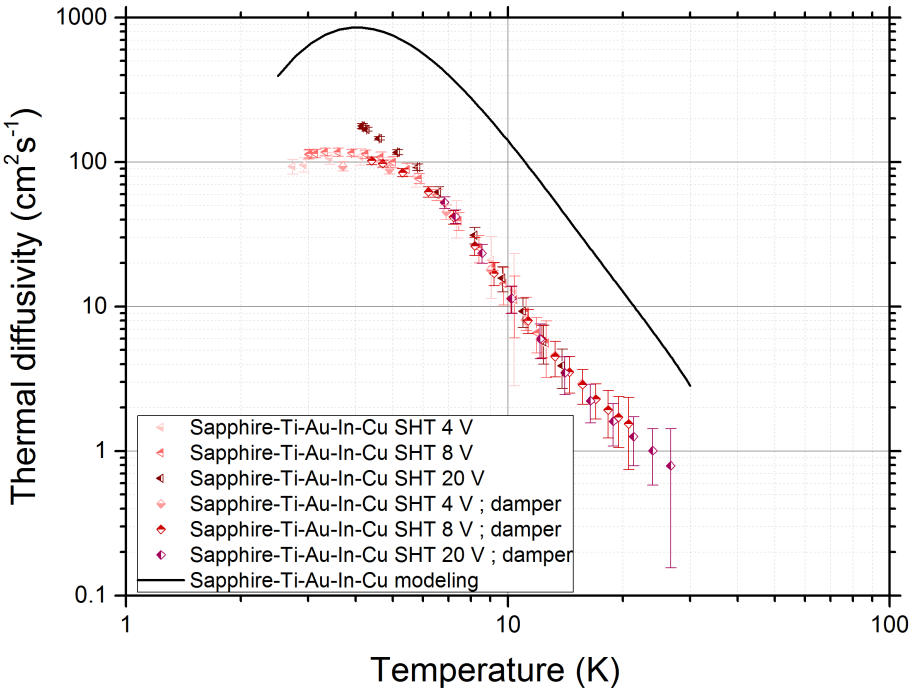

Figure 5.9: Comparison between measured and modeled values for $D_s(T)$ of S2.

Based on the measurement and simulation of the thermal conductivity the difference can only come from the heat capacity. The mock-up stores more heat than expected from the described model. The reason might be the increasing cross section or maybe the interfaces. It is also possible that the thermal diffusivity at the plateau is not the right value to take. The thermal diffusivity increases afterwards, maybe another plateau can be found at higher frequencies. The difference is discussed in more detail in the next section.

5.1.3. Interpretation

The schematic curve of the thermal diffusivity versus frequency, observed for the sandwich measurements, is illustrated in Figure 5.10 and divided into three regions. The thermal diffusivity below the first threshold frequency f_{c1} is marked with 1. The thermal diffusivity at low frequencies can be strongly influenced by the additional heat capacities at the thermal link between cold head and experimental platform. For frequencies above f_{c1} one finds a plateau with constant thermal diffusivity values. The plateau cannot be found for all measurements and its value differs from the thermal diffusivity expected from the modeling. The region for frequencies higher than the second threshold frequency f_{c2} is marked with 2. In that region the measured thermal diffusivity increases again. The frequency dependence of the thermal diffusivity was not expected and the effects in region 1 and 2 have to be discussed. Furthermore, the difference between model and measurements has to be interpreted.

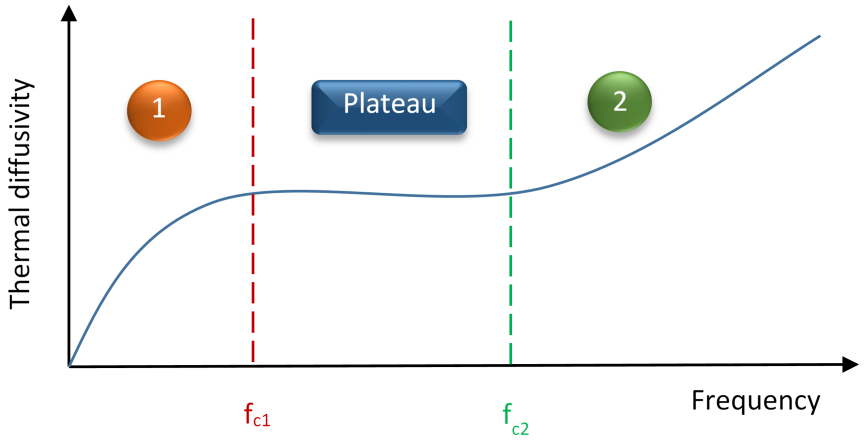

Figure 5.10: Typical curve shape for the frequency dependence of the thermal diffusivity.

Region 1 and damper influence

The frequency dependence in region 1 and the first threshold frequency were already observed for the reference sample. There, the influence of the components of the measurement apparatus on f_{c1} was visible by plotting f_{c1} versus temperature. A clear change in slope of the curve was found, were the measurement apparatus was changed from cryocooler to the vacuum chamber immersed in the refrigerant.
The sandwich at low temperatures was only measured in the cryocooler but the apparatus was changed by adding an additional heat capacity between experimental platform and cold head, the lead damper. That increase in heat capacity significantly changed the frequency behavior in region 1. In fact, for some curves the frequency dependence in that region completely vanishes or changes the sign of slope. The influence of the damper is significant but it does not effect the height of the plateau. Figure 5.11 shows a direct comparison between the measurements with and without damper at similar temperatures. For the curve at 7.3 K the thermal diffusivity is constant in region 1 and for curves at lower temperatures the slope changes from positive to negative, see Figure 5.3, Figure 5.4 and Figure A.4, Figure A.5. The temperature where the change in curve shape occurs is below 7.3 K, close to the transition temperature of lead (T $\sim$ 7.2 K [44]). But this is the temperature measured at the sample and the temperature at the lead damper is even lower. Hence, the lead damper is superconducting and the thermal conductivity and the heat capacity of lead are smaller than in normal conducting case [40]. The high influence of changes of the apparatus raises the question, weather the sample is measured or the sample including all the components connecting it to the cold head.
F. Pobell describes in [11] the AC calorimetry and mentions a first threshold frequency for his set-up. He describes it as frequency below which "heat escapes through the thermal link to the bath within the measuring period". Furthermore, he recommends a different design for the AC measurements on small samples, a calorimeter weakly coupled to the

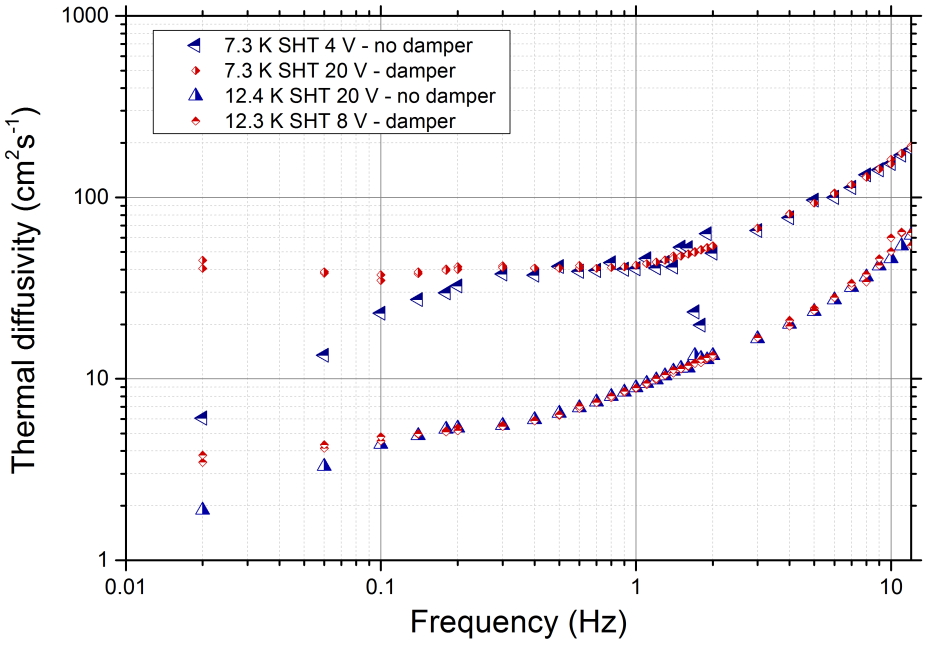

Figure 5.11: Frequency dependence of thermal diffusivity with and without damper.

thermal bath, realized by a sample holder hanging in vacuum by means of thin supporting wires. The heat capacity of the addenda should be significantly smaller than the heat capacity of the sample, or at least well known. Details can be found in [11]. Pobell describes a different experimental set-up than the one tested here, since the experimental platform is connected to the cold head by copper elements as shown in section 3.1. An adaption of the set-up due to Pobell's recommendations might help to reach the plateau at lower frequencies. This seems to be confirmed by the results obtained using the damper.

Region 2

The second increase of thermal diffusivity with frequency is surprising and it is not clear whether it is a real physical process or if it is just a measurement problem. Accuracy problems are caused by the small temperature amplitudes of just a few milliKelvin at high frequencies. Noise might influence the measurement and can cause inaccuracies. An offset in amplitude of 1 mK would not affect the measurements at low frequencies because of the high amplitude, but the influence of an offset would increase with increasing frequency and would consequently lead to an increase in measured thermal diffusivity. Figure 5.12 shows how an offset in amplitude would influence the shape of the $D_s(f)$ curve. To model these curves the measurement at 7.3 K with a SHT voltage of 20 V and the use of a damper was adapted. The measured thermal diffusivity at this temperature was shown in Figure 5.11. The measured amplitude $A(0)$ is used and the theoretical amplitude after crossing the sample $A(x)$ was calculated assuming a constant thermal diffusivity of 39 $\mathrm{cm^2/s}$. Thus,

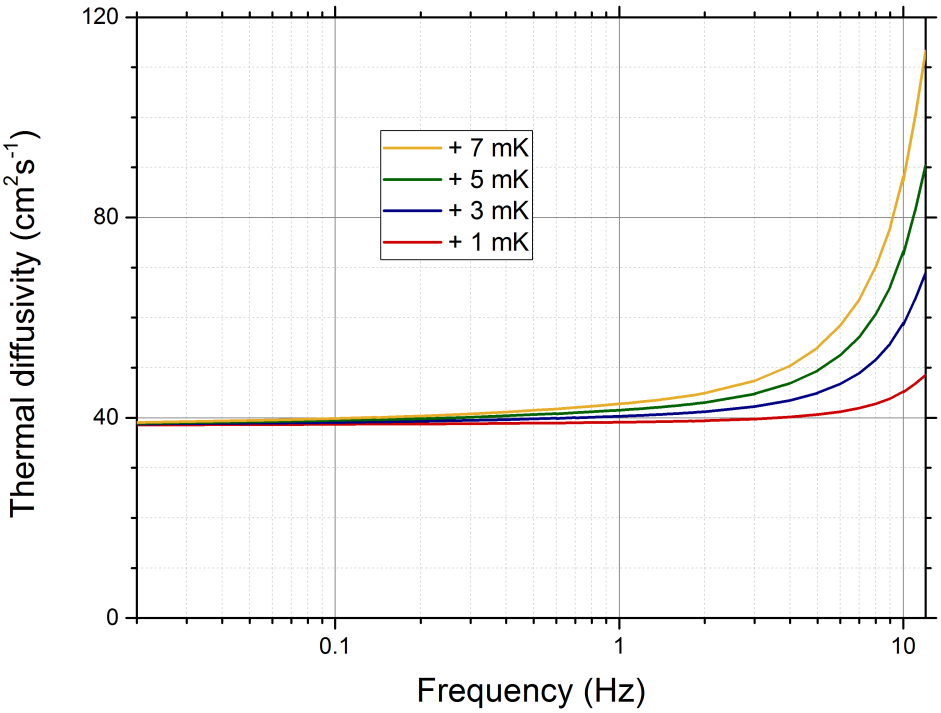

Figure 5.12: Plot of the calculated $D_s(f)$ with an amplitude offset.

the thermal diffusivity calculated from the amplitude ratio is a constant line. Now, to each of these amplitudes an error of +1 mK, +3 mK, +5 mK and +7 mK was added and the thermal diffusivity calculated. The following figures shows the result and the permanent increase in thermal diffusivity caused by the measurement errors. An offset of only 1 mK would already increase the thermal diffusivity from 39 cm^2/s to 50 cm^2/s at 12 Hz. The strong influence makes it clear that a measurement at low frequencies would be favorable.

Another explanation for the increase in thermal diffusivity could be the changing temperature gradient during the measurement. The amplitudes of the oscillations decrease with increasing frequency. Consequently, the temperature gradient between the sensors when the temperature wave reaches its maximum ΔT_{max} changes with frequency, too. Thermal resistance of a bulk material and the thermal boundary resistance are both dependent on $1/\Delta T$ as seen before. Considering a decreasing ΔT over the sandwich structure for the same $\dot{Q}$ would mean a higher thermal conductivity and, consequently, an increase in the thermal diffusivity based on the dynamic behavior of the material.

Figure 5.13 (left) shows a thermal diffusivity plot for S2 with and without the use of the damper. The graph right shows the $1/\Delta T_{max}$ behavior over frequency for the same sandwich. Both graphs have a similar behavior and even the plateau is visible in the right graph. The behavior was also plotted for S1 and can be found in the appendix, see Figure A.6. The decrease in ΔT_{max} becomes significant for high frequencies and the

observations make again clear that a measurement at low frequencies is more reliable, if one succeeds at lowering the first threshold frequency by adaption of the measurement apparatus.

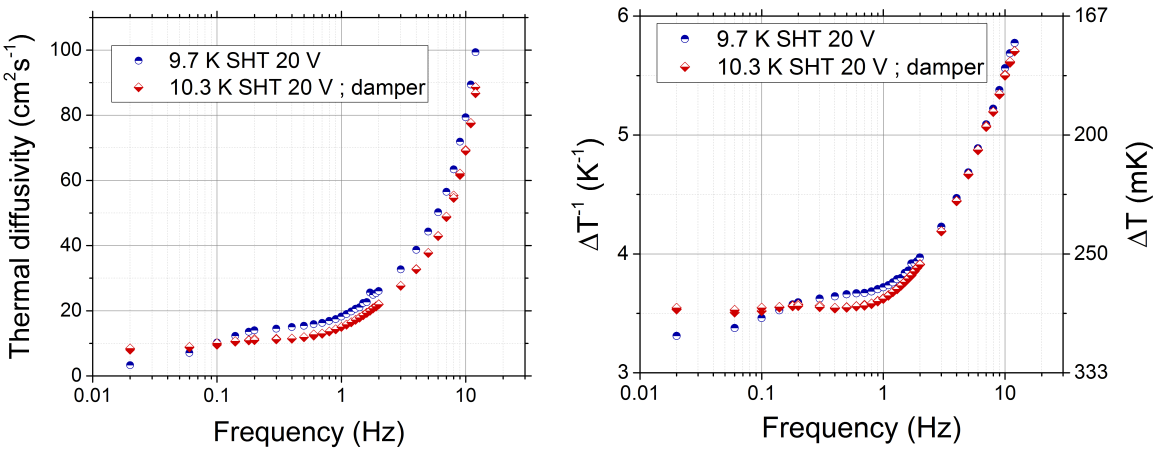

Figure 5.13: Plot of the frequency dependence of the thermal diffusivity (left) and ΔT_{max}^{-1} for S2 (right).

Plateau and difference between modeled and measured thermal diffusivity

There are two possibilities for the difference between model and measurement. Either the model might not include all effects at interface up to now or the measurement includes deviations not accounted for.

(a) Measurement deviations

One possibility of a measurement influence was already discussed. It is possible that the sample plus the support structure (copper, damper) was measured, which would decrease the thermal diffusivity values. Yet, this possibility can be excluded. Copper was measured with the same apparatus and good results according to literature were obtained at the plateau. The dominating component of the sandwich is also copper, thus, the conditions should not differ significantly.
Another presumption could be that the waiting time between two measurements was not long enough so the sample could not heat up to a stable temperature. That could result in different thermal diffusivity values.

(b) Model improvement

The thermal conductivity was measured and modeled in the sense that it matches the

truth. The thermal conductivity already includes the thermal boundary resistance, thus, further effects due to the interface are not expected. Regarding the measurement values, the heat capacities should be higher than used in the model. Since the copper bar was measured with the same addenda, heat capacities from the apparatus should not be of importance. What was not considered in the model was the changing cross section of the sandwich mock-up. For the modeling either the whole volume of the sandwich V_{total} or the volume in direct line of heat transport V_{direct} was considered. Both volumes are illustrated in Figure 5.14. Both assumptions gave nearly the same results for the final modeled thermal diffusivity, i.e., one gets the same result for the heat capacity weather all the measured volume is direct in line of the heat transport or not. That fact is problematic.

As an example one could take the volume of the copper platform and imagine it as a thin layer with the same volume as before. From the modeling one would get the same thermal diffusivity as for the mock-up shown here, because of the constant volume. But that assumption might be wrong since one would have to consider a conduction process as two dimensional.

It is possible that the ratio between the total volume V_{total} and the volume in direct line of the heat transport V_{direct} needs to be considered. Calculating the ratio V_{total}/V_{direct} for the sandwich mock-up the geometry factor is 3.3 for S1 and 2.7 for S2, see Figure 5.14. Since the mass of copper is dominating, the same numbers will be obtained considering the mass ratio. The additional mass might store the heat, but it is not in line of the heat conduction from one to the other side of the sandwich and does not contribute to it.

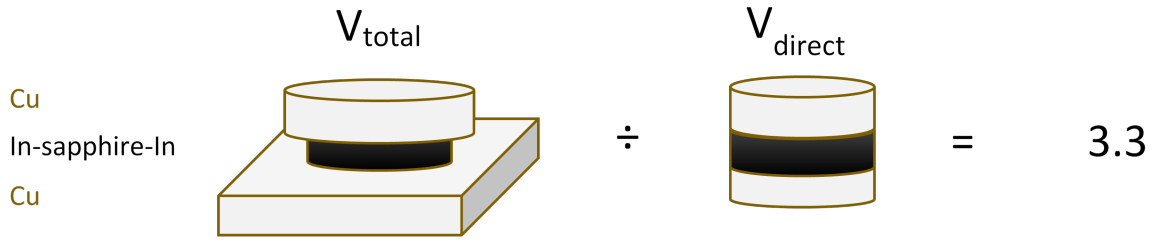

Figure 5.14: Schmematic of the geometry factor for S1.

A geometry factor could explain why the thermal diffusivity of the reference sample agrees with literature values. There, the cross section was constant over the whole sample. Dividing the modeled thermal diffusivity values by the calculated geometry factor of each mock-up gives the result shown in Figure 5.15. The agreement between model and measurement is much better for the sapphire-indium-copper sandwich. A difference between model and measurement is still visible at the maximum. For the model 99.99 % copper was used. Using less pure copper would decrease the thermal diffusivity at the peak. The agreement between measurement and modeling with geometry factor for S2 is not as suc-

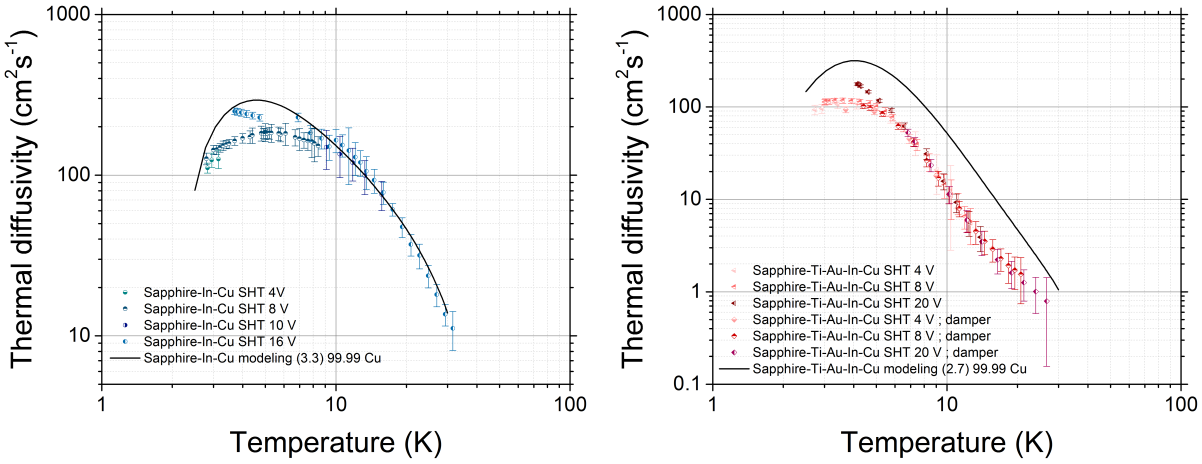

Figure 5.15: Plot of $D_s(T)$ for S1 (left) and S2 (right) measured and modeled with the geometry factor.

cessful as for S1. The values still differ by a factor 3, but seem to merge at a temperature of about 3 K. The same temperatures where the thermal diffusivity curves of S1 and S2 merged.

There are two possibilities to explain the difference between S1 and S2. One idea could be that a less pure copper or differently treated copper is used for S2 than for S1. First, that explains why the measured thermal conductivity curves of S1 and S2 are different at high temperatures and why the curves merge at low temperatures. As described in section 2.2 the purity of a material defines the temperature and value of the maximum in thermal conductivity. The mean free path of the electrons increases until it reaches the dimension of the lattice defect distance and stays constant with decreasing temperature. At that point the thermal conductivity of a pure metal becomes proportional to temperature and the thermal diffusivity becomes constant. That the purity of copper can influence the thermal diffusivity by orders of magnitude is illustrated in the appendix, see Figure A.7. For the sandwich the thermal boundary resistance and effects of the other sandwich elements might influence that behavior. At temperatures below the maximum in thermal conductivity the only temperature dependent unit left, which can decrease the thermal diffusivity of a sandwich, is the thermal boundary resistance, as discussed in section 2.4. The same thermal conductivity and diffusivity for S1 and S2 at low temperatures might indicate that the thermal boundary resistance of both sandwiches is the same. This would mean the titanium-gold layer would not affect the thermal properties of the sandwich at low temperatures.

Another assumption could be an additional heat capacity based on the boundaries at temperatures below the peak in thermal diffusivity. Such an effect is not known in literature, but could explain the difference between model and measurement. It would also explain that the effect is stronger on S2 compared to S1, based on the additional boundaries.

Further investigation is necessary to study the geometry factor. The same sandwich but with a constant cross section should be studied. It should be made sure the copper is handled the same way in terms of machining and heat treatment. Furthermore, more layers should be added to the described set-up to study if the difference between model and measurement increases further.

5.2. Measurements at ultra-low temperatures

Both sandwich structures were measured at ultra-low temperatures in the described dilution refrigerator from section 3.2. The measurement chain and temperature sensor types are described in section 4.1. The sapphire-indium-copper sandwich was only measured at frequencies below 1/15 Hz because it was studied before the investigation of the measurement method. At that time it was not known that a plateau can be found at higher frequencies. Therefore, all the results are frequency dependent and shall not be discussed here. The platform with the sapphire-titanium-gold-indium-copper is mounted on the mixing chamber lid as shown in Figure 5.16. To reach different temperature ranges, the mixing chamber temperature (TMC) was heated and stabilized at 30 mK, 50 mK, 100 mK, 180 mK and 250 mK. The measurement procedure is the same as described at low temperatures. A sinusoidal heat signal is applied up to 3 Hz. At higher frequencies the signal is too noisy for the thermal diffusivity measurements. The sensors are measured subsequently based on the different ranges required for the AC resistance bridge. Titanium and indium are both superconducting (sc) below 400 mK. Therefore, a magnetic field of about 32.3 mT [1] was generated to suppress superconductivity in both materials and to measure the normal conducting (nc) case.

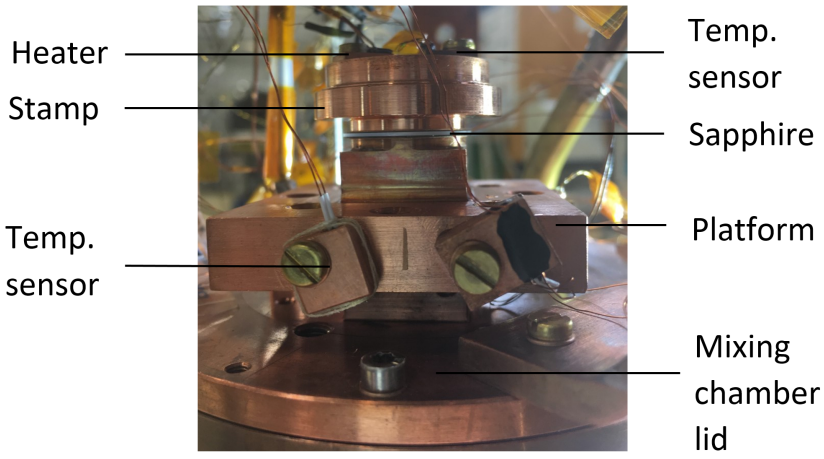

Figure 5.16: Picture of the S2 sandwich mounted on the mixing chamber of the dilution refrigerator.

5.2.1. Results

The search for the plateau in the milliKelvin temperature range is very challenging. A high amplitude compared to the absolute temperature has to be applied to the sandwich. The platform is coupled to the mixing chamber copper lid via a copper block. As discussed before, that may increase the first threshold frequency. The plateaus are almost not visible in the normal conducting case. Because of noisy sensor signals the second threshold frequency is very low. Consequently, f_{c1} and f_{c2} overlapped for many measurements and either no plateau, only an inflection point, or nothing can be detected. In normal conducting case an inflection point at 45 mK and 93 mK can be found, see Figure 5.17. The temperature is again the mean between platform and stamp

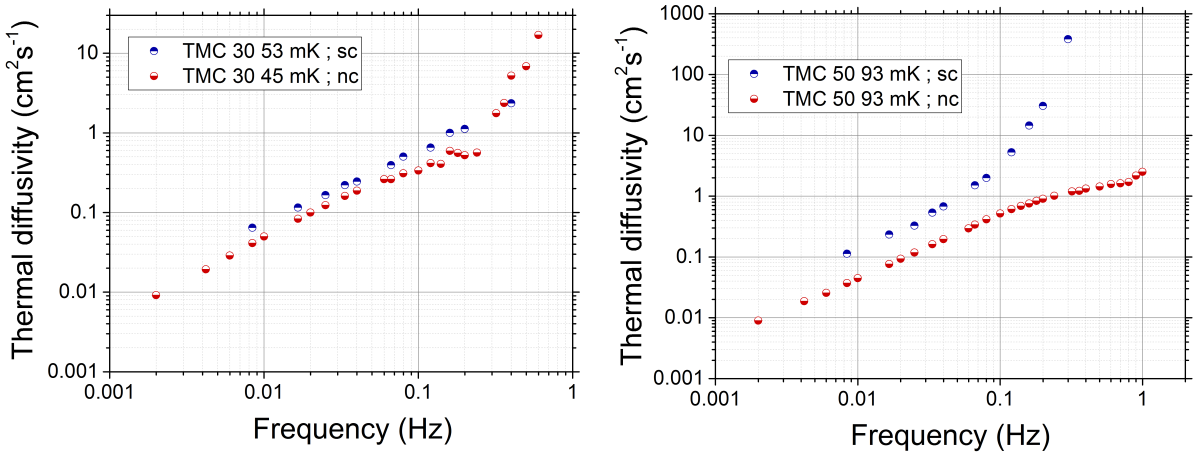

Figure 5.17: Plot of $D_s(f)$ for S2 sc and nc at TMC 30 mK (left) and TMC 50 mK (right).

temperature. The thermal diffusivity at these points can be determined as D_s (45 mK) = (0.5 ± 0.1) cm²/s and D_s (93 mK)= (1.5 ± 0.2) cm²/s. The error bars are taken from the standard deviation around the inflection points. It was not possible to detect an inflection point or plateau for measurements with mixing chamber temperatures of 30 mK and 50 mK in superconducting case. At higher temperatures the curves are more distinct in superconducting case and a plateau can be found for mean temperatures of 230 mK and 290 mK, see Figure 5.18. The thermal diffusivity at these points can be calculated as D_s (230 mK) = (1.2 ± 0.1) cm²/s and D_s (290 mK) = (1.4 ± 0.1) cm²/s. The thermal diffusivity is not stable for a wide frequency range and no further stable points were found in the milliKelvin temperature range. This is attributed to the overlap of threshold frequencies. Thus, only two measurement points for each case exist at ultra-low temperatures.

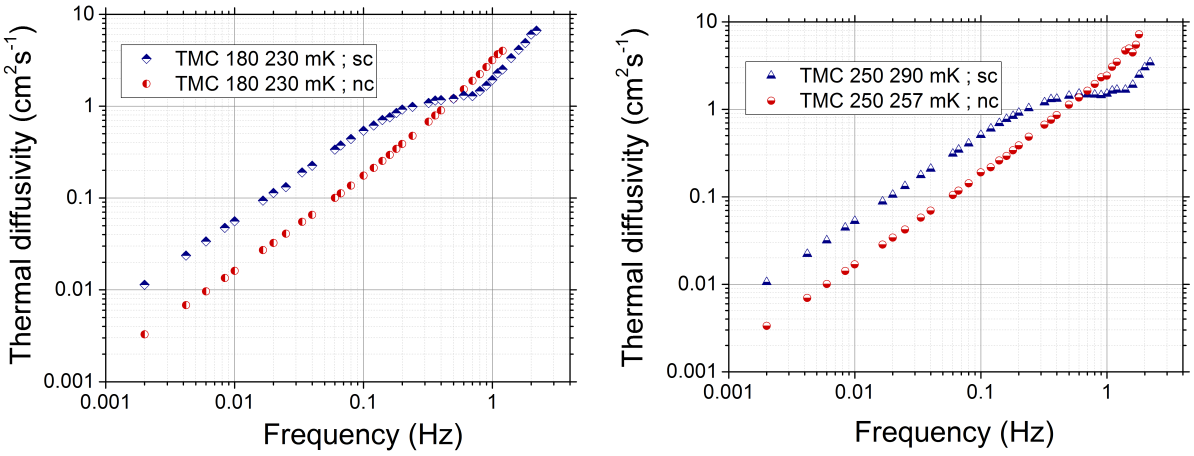

Figure 5.18: Plot of $D_s(f)$ for S2 sc and nc at TMC 180 mK (left) and TMC 250 mK (right).

5.2.2. Modeling

The modeling is performed as for the low temperature measurements, see section 5.1.2. First, the thermal conductivity at ultra low temperatures is studied (measurement performed by J. Liberadzka) and analyzed in normal conducting and superconducting case. The thermal conductivity of the sapphire-titanium-gold-indium-copper sandwich plotted over the whole temperature range can be found in the appendix, see Figure A.9. Afterwards, the specific heat is modeled from literature values for sapphire, copper and indium [11] as described before. The specific heat of titanium and gold was neglected for the modeling. Both layers are very thin and do not contribute much to the total heat capacity.

The modeling results for the thermal diffusivity are again higher than the measurement results. Applying the suggested geometry factor of 2.7 to consider the mass difference, measurement and modeling of S2 show a good agreement for normal conducting and superconducting case. The results of the modeling with the geometry factor and the measured thermal diffusivity are shown in Figure 5.19.

It is a fabulous match of model including geometry factor and measurement. The thermal diffusivity decreases with decreasing temperature. That proofs the strong influence of the interfaces. In a bulk material the thermal diffusivity should be almost constant or slightly rising with decreasing temperature at ultra low temperatures. Small differences between model and measurement may come from the fitting and measurement inaccuracies for the thermal conductivity measurement. Furthermore, the geometry factor could have changed slightly, based on the bigger sensors bolted to the platform.

The thermal diffusivity is smaller in superconducting state than in normal conducting state. That is expected from the decrease in thermal conductivity because heat carriers in the metal are bound in Cooper pairs in superconducting state.

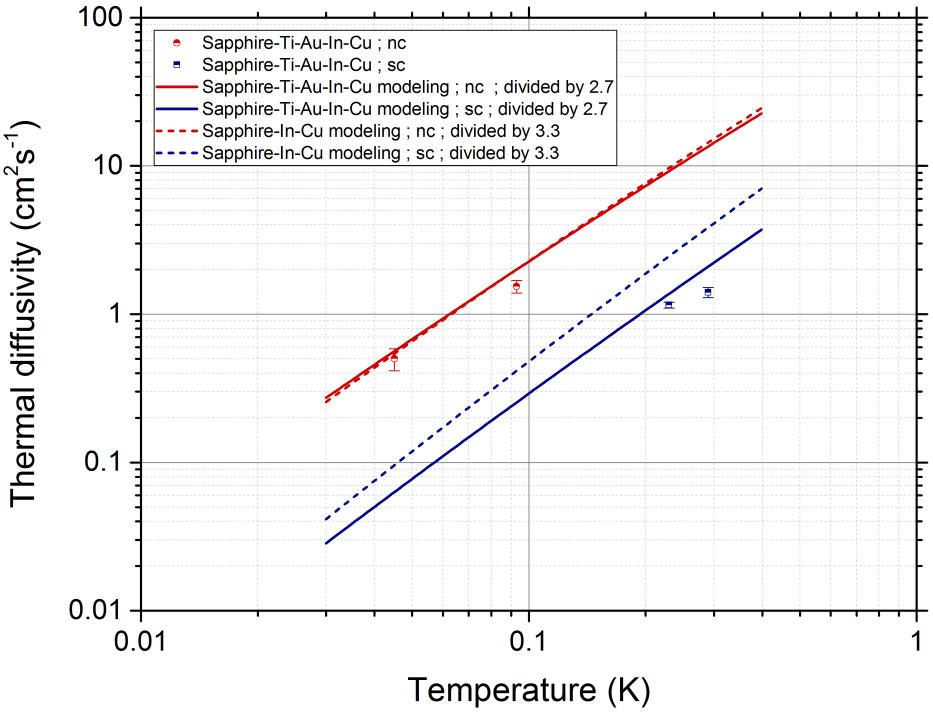

Figure 5.19: Plot of the temperature dependence at ultra-low temperatures of thermal diffusivity modeled with geometry factor for S1 and S2 and measurement points for S2 sandwich set-up.

Based on the good agreement between model and measurement for the sapphire-titanium-gold-indium-copper sandwich, a model including the geometry factor is also performed for the sapphire-indium-copper sandwich. The results obtained for the thermal conductivity measurement can be found in the appendix, see Figure A.8. The final modeled thermal diffusivity is added as dotted line in Figure 5.19. Measurement results do not exist. The resulting curves for the normal conducting case overlap, which could mean the same thermal boundary resistance for S1 and S2. The thermal diffusivity of both sandwich mock-ups is smaller for the superconducting case than for the normal conducting case but the curves obtained from S1 and S2 do not overlap.

5.2.3. Interpretation

Figure 5.20 shows all measurement data and the modeling data without geometry factor for sandwich S1 and S2 for the whole temperature range between 30 mK and 30 K for the normal conducting case. At ultra-low temperatures the modeling with the geometry factor gives results in good agreement with the measurement for the sandwich mock-up S2, see Figure 5.19. Without the geometry factor there is a difference between model and measurement. Possible reasons for the difference were already discussed in section 5.1.3. The strong influence of the thermal boundary resistance is visible for both sandwich mock-

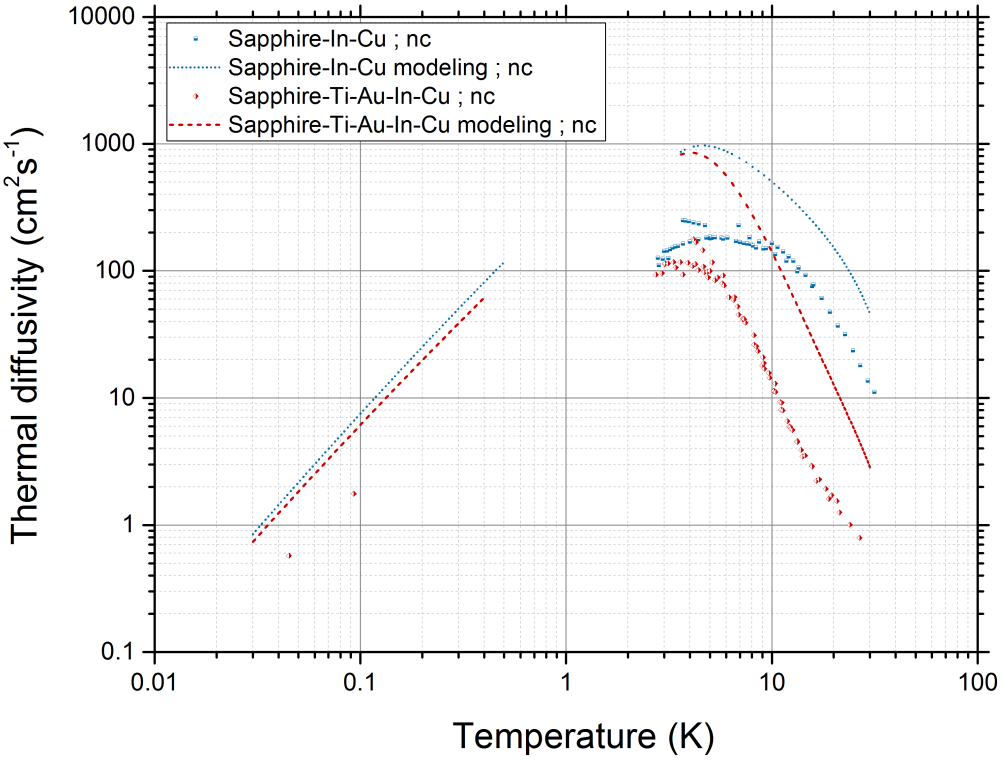

Figure 5.20: Plot of the temperature dependence of the thermal diffusivity of S1 and S2 measured and modeled without geometry factor between 30 mK and 30 K.

ups. Without the thermal boundary resistance the thermal diffusivity would increase towards low temperatures until the mean free path is constant. Combining equation (6) and (18) it becomes obvious that the thermal diffusivity is almost constant when the mean free path is constant. The decrease of the thermal diffusivity towards ultra-low temperatures proofs the expected strong influence of the thermal boundary resistance.
Thermal diffusivity in superconducting state at ultra-low temperatures for sandwich S2 is always smaller than for S1 as expected due to the additional superconducting layer, see Figure 5.19. The measured thermal conductivity used for the modeling of the thermal diffusivity for S1 and S2 in the superconducting state can be found in the appendix, see Figure A.11. The thermal conductivity of both samples differs at about 300 mK and the difference vanishes at about 50 mK. A smaller thermal conductivity of S2 is visible as expected. The sandwich has an additional superconductor because of the titanium layer, due to that electrons are bound in Cooper pairs too and the thermal conductivity of the stack decreases. The reason for the consolidation of the two curves is not yet clear. At about 50 mK the temperature sensor signal was very noisy, that might have influenced the measurement or a self-heating effect which affects the measurement more strongly at low temperatures could have caused this effect.
To decide which sandwich is more suitable for AEgIS only the normal conducting state

needs to be considered. The thermal diffusivity of both sandwich mock-ups S1 and S2 at ultra-low temperatures is the same (modeling including geometry factor) or the thermal diffusivity is slightly higher for S1 than for S2 (modeling without geometry factor) in normal conducting case. The two experimental curves already merged at about 3 K. Furthermore, the thermal conductivity at ultra low temperatures is almost the same for sandwich mock-ups S1 and S2 in normal conducting case, see Figure A.10.
A more significant difference between sandwich S1 and S2 was expected at ultra-low temperatures because for the sandwich mock-up S2 the boundaries changed and an additional boundary was added compared to S1. An indium layer was exchanged with a thin titanium-gold layer for S2. Consequently, instead of a indium-indium boundary there is now an indium-gold boundary and instead of the indium-sapphire boundary a titanium-sapphire boundary. The additional boundary is the boundary between titanium and gold. The acoustic properties of indium ($v_L = 2.699 \cdot 10^5$ cm/s, $v_T = 0.905 \cdot 10^5$ cm/s) [19] and gold ($v_L = 3.39 \cdot 10^5$ cm/s, $v_T = 1.29 \cdot 10^5$ cm/s) [19] do not differ significantly and as before it is a boundary between two metals. The acoustic properties of sapphire ($v_L = 10.89 \cdot 10^5$ cm/s, $v_T = 6.45 \cdot 10^5$ cm/s) [19] and titanium ($v_L = 6.070 \cdot 10^5$ cm/s, $v_T = 3.125 \cdot 10^5$ cm/s) [45] differ significantly, but the difference is smaller than for an indium-sapphire boundary. That change might be even advantageous and may negate the influence of the additional titanium-gold boundary in the sandwich S2. Thus, a similar or the same thermal diffusivity for S1 and S2 at ultra-low temperatures is possible.
But one has to be careful comparing the thermal diffusivity of sandwich S1 and S2 and draw conclusions for the thermal boundary resistance. The thermal diffusivity is dependent on the distance between the two temperature sensors, but the distance is not the same for the sandwich mock-up S1 (d = 1.975 cm) and S2 (d = 2.775 cm). To calculate the final thermal diffusivity the factor calculated from the amplitude attenuation over the sandwich structure is multiplied with the squared distance, see equation (27). But most of the amplitude attenuation at ultra-low temperatures happens at the boundary, consequently the additional distance for S2 should not be considered for the comparison of the thermal diffusivity. By doing this, one gets a factor of about 2 ($(2.775\text{ cm})^2/(1.975\text{ cm})^2 \approx 2$). That means the additional boundary at sandwich S2 increases the thermal boundary resistance by a factor of about 2. That assumption ignores thermal resistivity and heat capacity of the 0.8 cm copper block for S2. The thermal resistivity can be neglected due to the high thermal conductivity of copper at ultra-low temperatures but the modeling showed that additional heat capacities can not be neglected. So in reality the factor is below 2. The exact values for the thermal boundary resistances of sandwich S1 and S2 will be determined by J. Liberadzka in her doctoral thesis.
Based on the fact that only four measurement points of the thermal diffusivity exist for S2 and no points for S1 at ultra-low temperatures, the measurement should be repeated at ultra-low temperatures with the same distance between the temperature sensors to

confirm the modeled values.
But from the results obtained up to now one sees already clearly that the additional boundary for sandwich S2 increases the thermal boundary resistance. Consequently, sandwich S1 is the better choice.

6. Conclusion and outlook

The objectives of the thesis, to study the AC measurement method and use it to obtain the thermal diffusivity for sandwich structures that consist of different materials in series, have been achieved. Two sandwich structures were investigated, varying in the amount and the material of the interfaces. It was relevant to detect which of these structures can transport heat loads the fastest to the mixing chamber of a dilution refrigerator in order to decide which sandwich structure is most suitable for AEgIS.
Based on the measurements performed in the thesis, many characteristics of the AC method were detected. Two values, obtained with the measurement of a sinusoidal heat signal, can be analyzed to determine the thermal diffusivity - the phase shift and the amplitude attenuation. It has been proven that the phase shift method is not suitable for measurements on the sandwich in a dilution refrigerator, since an AC resistance bridge is necessary for these studies. The resistance bridge causes an additional phase shift. Moreover, the accuracy of the method is not high enough to measure the small phase shifts expected for the samples. It was also shown that the previous measurements performed by C. van der Post [10] using the AC amplitude method were measured correctly, but at too low frequencies. The frequency dependence of the method is clearly visible for all samples and a correct measurement is only possible in a small frequency range where the thermal diffusivity is constant. Ideas where the frequency dependence originates from and how the constant "plateau" could be extended to lower frequencies were discussed.
The thermal diffusivity for both sandwich structures was measured between 3 K and 30 K and it was evident that the thermal diffusivity is the same for both sandwich mock-ups at about 3 K. Because of different sensor distances for S1 and S2 the same thermal diffusivity means a higher thermal boundary resistance of about factor 2 for sandwich S2 caused by the additional metallic boundaries as discussed in section 5.2.3.
Unfortunately only one sandwich structure was measured successfully at ultra-low temperatures. Only two reliable measurement points in normal conducting and superconducting state for the sapphire-titanium-gold-indium-copper sandwich have been obtained.
To gain information about the thermal diffusivity at ultra-low temperatures and to check the validity of the measurements, the thermal diffusivity for both sandwiches was modeled. The modeled curve has the same shape as the measured curve but the absolute values differ by a factor of 3 to 6. Possible reasons for the discrepancy, such as geometry

factor or copper purity, were discussed.
The modeled thermal diffusivity at ultra-low temperatures, which is based on measurements of the thermal conductivity in the same temperature range, shows depending on the model, no or only small differences in thermal diffusivity between the two sandwich mock-ups. That result confirms the outcome from the low temperature thermal diffusivity measurements and means an increase of the thermal boundary resistance of sandwich S2 by a factor of about 2. For the AEgIS experiment, it can be concluded that the sandwich structure S1 is more suitable for the thermal link between the electrode and the mixing chamber lid.
Future measurements should study the proposed geometry factor by comparing measurements of the same, well known material shaped differently. Furthermore, the studies at ultra-low temperatures should be repeated for the sapphire-indium-copper sandwich, to see if they confirm the modeled values. For new thermal diffusivity measurements the recommendations by F. Pobell in [11] should be tested, to see if a stable thermal diffusivity can be achieved at low frequencies. Finally, the results obtained with the adapted apparatus should be compared to measurements with the original set-up, to see if the absolute values are the same.

A. Appendix

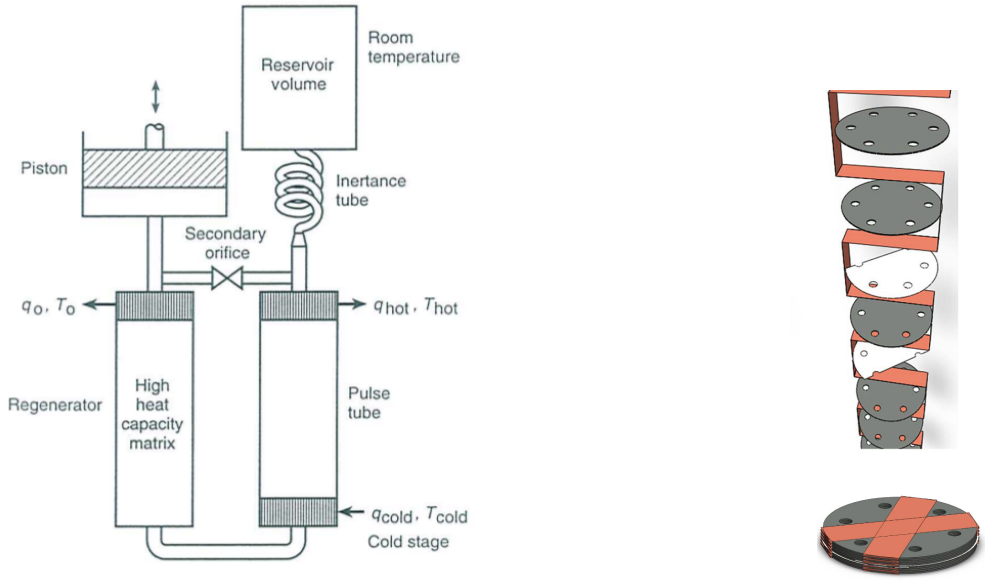

Figure A.1: Basic elements of a double inlet pulse-tube cryocooler [17] (left) and the additional applied thermal damper (right) [33].

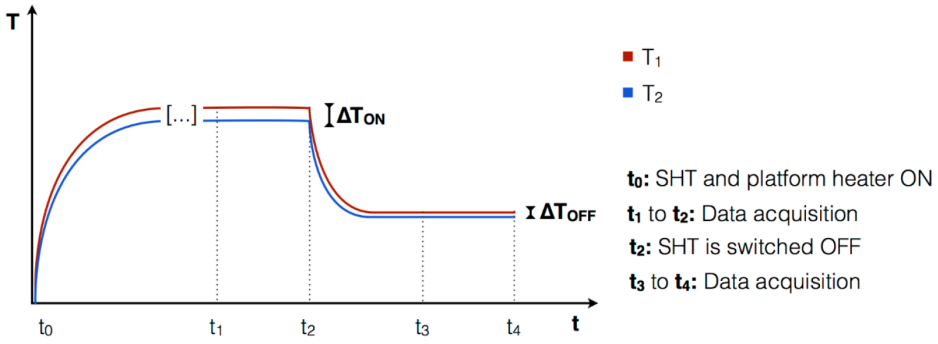

Figure A.2: Typical warm-up and cool-down curve for steady state measurements [34] used to calculate the thermal conductivity of both sandwich mock-ups.

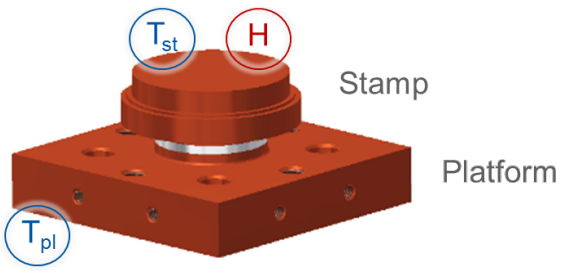

Figure A.3: Mock-up for sandwich S1 with temperatures sensors T and heater H positions [36].

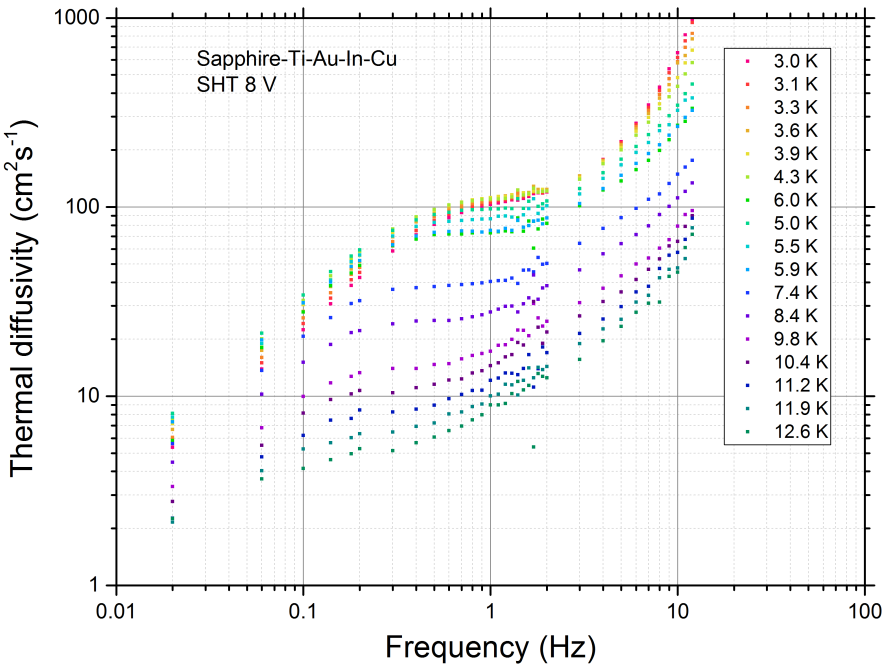

Figure A.4: Plot of $D_s(f)$ for S2 measured without the damper for 8 V SHT voltage (temperature decreases from bottom curve to top curve).

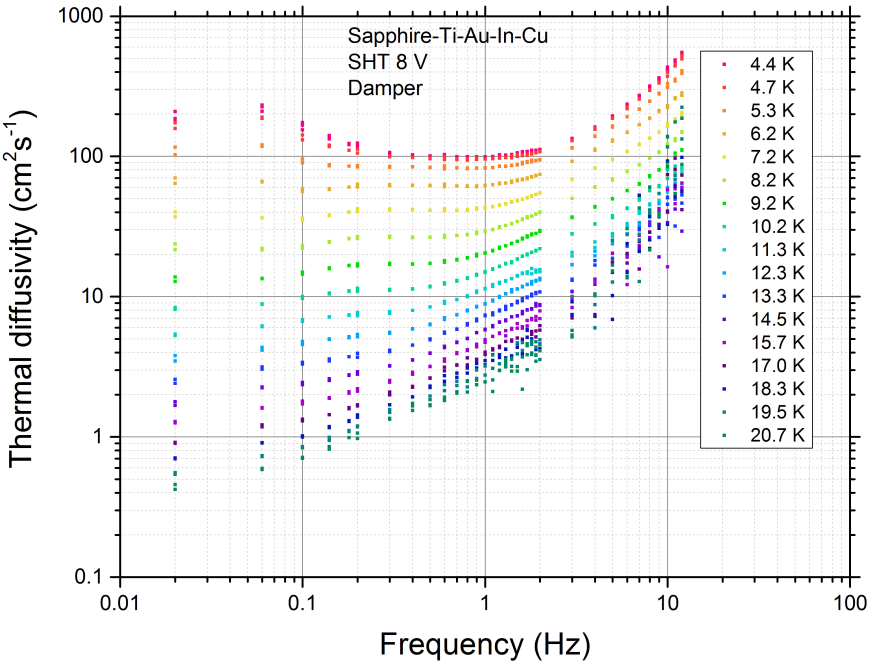

Figure A.5: Plot of $D_s(f)$ for S2 measured with the damper for 8 V SHT voltage (temperature decreases from bottom curve to top curve).

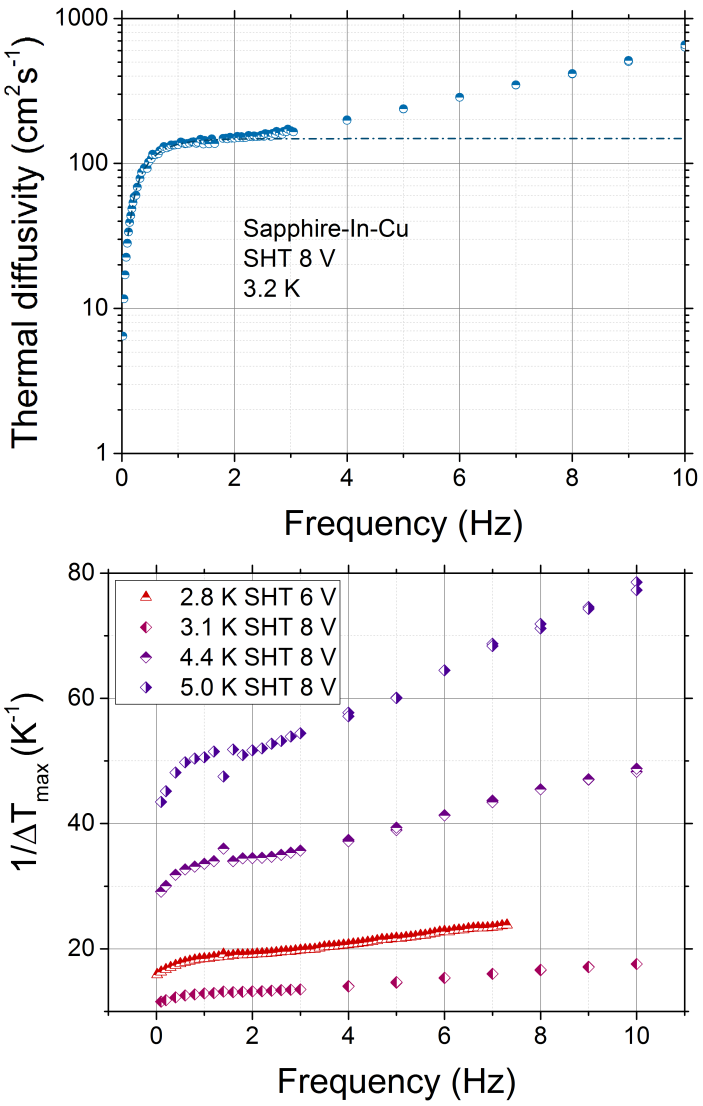

Figure A.6: Frequency dependence of the thermal diffusivity (top) and $1/\Delta T_{max}$ (bottom) for S1.

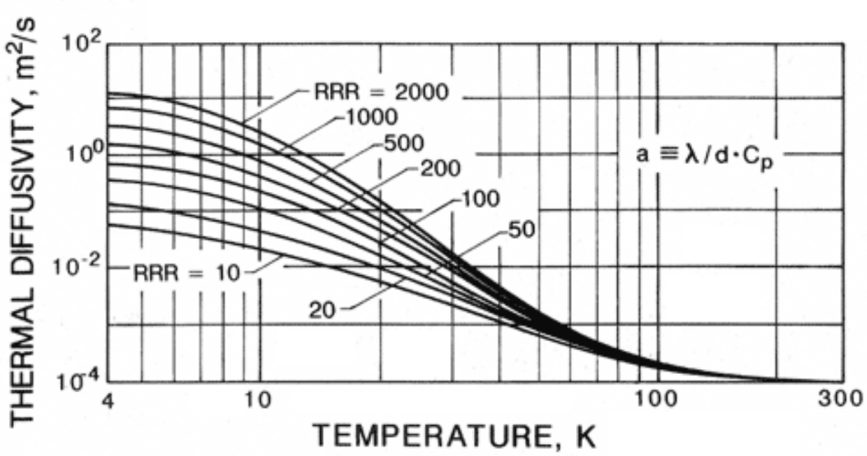

Figure A.7: Thermal diffusivity of different copper qualities [46].

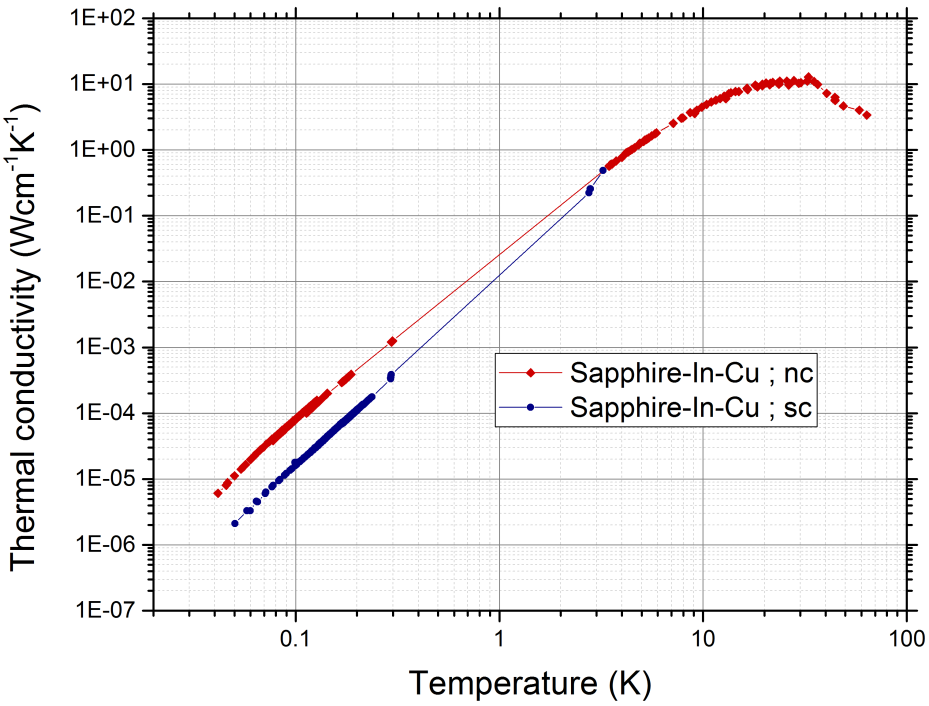

Figure A.8: Temperature dependence of the thermal conductivity for sandwich S1 measured between 30 mK and 60 K for normal and superconducting state.

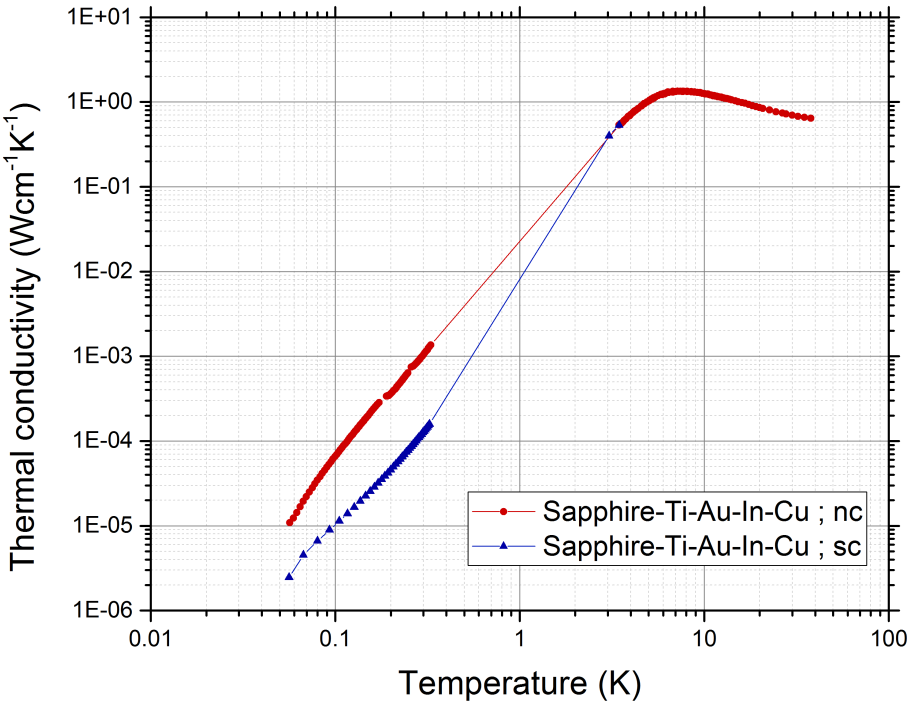

Figure A.9: Temperature dependence of the thermal conductivity for sandwich S2 measured between 30 mK and 30 K for normal and superconducting state.

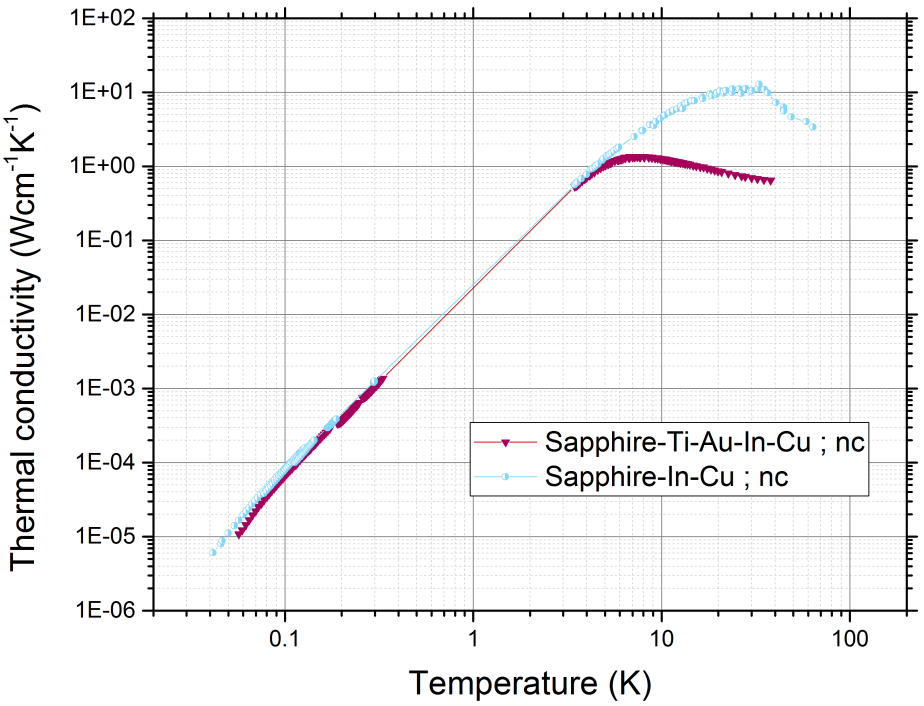

Figure A.10: Comparison of thermal conductivity versus temperature for sandwich S1 and S2 measured between 30 mK and 60 K in normal conducting state.

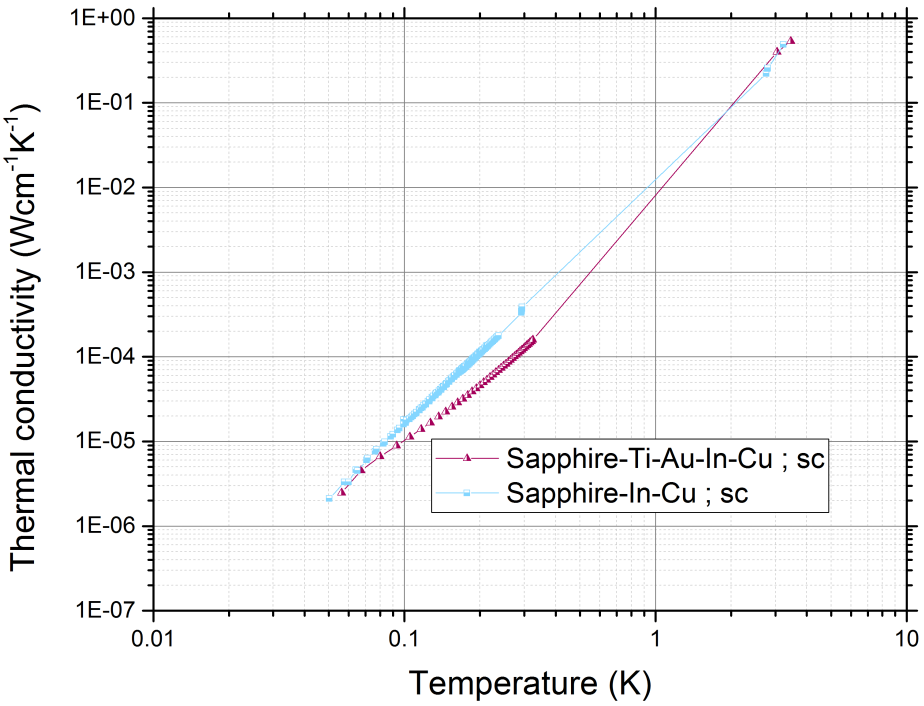

Figure A.11: Comparison of thermal conductivity versus temperature for sandwich S1 and S2 measured between 50 mK and 3 K in superconducting state.

References

[1] T. Eisel. Cooling of electrically insulated high voltage electrodes down to 30 mK. Dissertation. Technische Universität Dresden, 2011.

[2] V. Bouchiat et al. Measurement method of the antiproton gravitational mass using the single electron transistor. In: *Hyperfine Interact.* 109.1-4 (1997), pp. 345–355.

[3] W. Rosser. Introductory Special Relativity. Taylor & Francis, 1992.

[4] CERN Accelerator Complex. URL: `http://www.lhc-facts.ch/img/news2015/lhccomplex_.jpg` (visited on 10/26/2017).

[5] The Antiproton Decelerator. URL: `https://home.cern/about/accelerators/antiproton-decelerator` (visited on 11/02/2017).

[6] A. Kellerbauer et al. Proposed antimatter gravity measurement with an antihydrogen beam. In: *Nuclear Instruments and Methods in Physics Research B 266* (2008).

[7] M. Doser et al. Measuring the fall of antihydrogen: the AEgIS experiment at CERN. In: *Physics Prodedia 17* (2011).

[8] L. Smestad. Antimatter Research with the AEGIS Experiment- Probing Gravity with a Beam of Cold Antihydrogen. Presentation. Grav17 conference, Cordoba, Argentinia. 2017.

[9] J. Derking et al. Design and testing of 100 mK high-voltage electrodes for AEgIS. In: *ICEC 25–ICMC* (2014).

[10] C. C. W. van der Post. Heat Transfer at Ultra-Low Temperature. In: *Thesis* (2016).

[11] F. Pobell. Matter and Methods at Low Temperatures. Springer Berlin Heidelberg, 1995.

[12] W. Demtröder. Experimentalphysik 3. Springer Berlin Heidelberg, 2010.

[13] C. Enss and S. Hunklinger. Tieftemperaturphysik. Springer Berlin Heidelberg, 2000.

[14] C. P. Poole, H. A. Farach, and R. J. Creswick. Superconductivity. Academic Press, Inc., 1995.

[15] P. Seidel. Supraleitende Materialien. Lecture notes. 2018.

[16] H. Frey and R. A. Haefer. Tieftemperaturtechnologie. Verlag des Vereins Deutscher Ingenieure Düsseldorf, 1981.

[17] J. W. Ekin. Experimental Techniques for Low-Temperature Measurements. Oxford University Press, 2006.

[18] F14 Debye-Temperatur. URL: `http://www.kip.uni-heidelberg.de/fp/F14/FP14_Anleitung.pdf` (visited on 12/15/2017).

[19] E. T. Swartz and R. O. Pohl. Thermal boundary resistance. In: *J. Phys. D: Appl. Phys. 32* (1999).

[20] P. L. Kapitza. Heat Transfer and Superfluidity of Helium II. In: *Phys. Rev.* 60 (4 1941), pp. 354–355.

[21] G. Frossati. Experimental Techniques: Methods for Cooling Below 300 mK. In: 87 (1992).

[22] Kapitza Thermal Boundary Resistance. URL: `https://www.slideshare.net/thinfilmsworkshop/jay-amrit-kapitza-resistance-at-niobiumsuperfluid-he-interfaces` (visited on 12/13/2017).

[23] E. Gmelin et al. Thermal boundary resistance of mechanical contacts between solids at sub-ambient temperatures. In: *Reviews of Modern Physics, Vol. 61, No. 3* (1989).

[24] T. Okamoto et al. Electrical resistance of screw-fastened thermal joints for ultra-low temperatures. In: *Review of Scientific Instruments 61, 1332* (1990).

[25] R. Gross and A. Marx. Festkoerperphysik. Oldenbourg Wissenschaftsverlag, 2012.

[26] L. Salerno, P. Kittel, and A. Spivak. Thermal conductance of pressed metallic contacts augmented with indium foil or Apiezon grease at liquid helium temperatures. In: *Cryogenics* 34.8 (1994), pp. 649 –654.

[27] Y. Jun et al. Investigation of a Microcalorimeter for Thin-Film Heat Capacity Measurement. In: *Chinese Phys. Lett. 22 2429* (2005).

[28] E. Marin. Characteristic dimensions for heat transfer. In: *Lat. Am. J. Phys. Educ. Vol. 4* (2010).

[29] W. Czarnetzki and W. Roetzel. Temperature Oscillation Techniques for Simultaneous Measurement of Thermal Diffusivity and Conductivity. In: *International Journal of Thermophysics, Vol.16, No.2* (1995).

[30] T. Köttig. Dünnschichtsysteme für die effektive Tieftemperaturregeneration. Dissertation. Friedrich-Schiller-Universität Jena, 2007.

[31] P. Seidel. Applied superconductivity: handbook on devices and applications. Weinheim: Wiley-VCH, 2015.

[32] R. Radenbaugh. Refrigeration for superconductors. In: *Proceedings of the IEEE* 92.10 (2004), pp. 1719–1734.

[33] G. Dubuis, X. He, and I. Božović. Sub-millikelvin stabilization of a closed cycle cryocooler. In: *Review of Scientific Instruments* 85.10 (2014).

[34] P. Borges de Sousa. Thermal Conductivity of impregnated Nb3Sn coil samples CTD-101 K bulk sample. In: *CERN Measurement Report* (2016).

[35] J. Liberadzka and H. Derking. Ultra-cold electrodes for AEgIS. Presentation. 2013.

[36] J. Liberadzka. Heat Transfer at a Sapphire - Indium Interface in the 30 mK - 300 mK Temperature Range. Presentation. 2017.

[37] T. Eisel et al. Cooling of electrically insulated high voltage electrodes down to 30 mK – Dynamic measurements. In: *DKV-Tagung Magdeburg,AA I.02* (2010).

[38] J. Liberadzka, T. Koettig, et al. Heat transfer at a sapphire – indium interface in the 30 mK – 300 mK temperature range. In: *IOP Conf. Series: Materials Science and Engineering 171* (2017).

[39] *AVS-47B AC Resistance Bridge Instruction Manual*. Revised: 2015-11-02. PICOWATT. 2008.

[40] J. E. Jensen et al. Thermal Diffusivity. In: *Brookhaven National Laboratory Selected Cryogenic Data Notebook, Brookhaven National Laboratory* (1980).

[41] *Technical Specifications CERN. Oxygen-Free Electronic copper*.

[42] R. Berman, E. L. Foster, and J. M. Ziman. Thermal Conduction in Artificial Sapphire Crystals at Low Temperatures. I. Nearly Perfect Crystals. In: 231 (July 1955), pp. 130–144.

[43] B. Boerstoel, J. Zwart, and J. Hansen. The specific heat of palladium, platinum, gold and copper below 30 K. In: *Physica* 54.3 (1971), pp. 442 –458.

[44] S. Hunklinger. Festkörperphysik 5. De Gruyter Oldenbourg, Berlin/Boston, 2017.

[45] READE. Speeds of sound of the elements. URL: `https://www.reade.com/reade-resources/reference-educational/reade-reference-chart-chemical/-elements-data/4-speeds-of-sound-of-the-elements` (visited on 04/08/2018).

[46] Cryogenic Properties of Copper. URL: `https://www.copper.org/resources/properties/cryogenic/images/Thermal-Diffusivity.gif` (visited on 04/06/2018).

Eigenständigkeitserklärung

Hiermit erkläre ich, dass ich die vorliegende Masterarbeit selbstständig angefertigt habe. Es wurden nur die in der Arbeit ausdrücklich benannten Quellen und Hilfsmittel benutzt. Wörtlich oder sinngemäß übernommenes Gedankengut habe ich als solches kenntlich gemacht.

Ort, Datum	Unterschrift

Danksagung

Am Ende meiner Masterarbeit möchte ich mich bei all jenen bedanken, die durch fachliche oder persönliche Unterstützung zum Gelingen dieser Arbeit beigetragen haben.
Die vorliegende Masterarbeit ist in Zusammenarbeit der Arbeitsgruppe Tieftemperaturphysik an der Friedrich-Schiller-Universität Jena und dem Cryolab am CERN entstanden.
Mein großer Dank gehört Prof. Paul Seidel für die Ermöglichung und Betreuung dieser Masterarbeit in der Arbeitsgruppe Tieftemperaturphysik.
Besonderer Dank gilt auch Dr. Torsten Köttig für die Möglichkeit die Experimente im Cryolab durchzuführen sowie die hervorragende Unterstützung und die Betreuung der Arbeit.
Für die wunderbare Zusammenarbeit und die Hilfe bei den zahlreichen Messungen am Mischungskryostaten und am Cryocooler gilt mein Dank Joanna Liberadzka und Dr. Patricia Borges De Sousa.
Des Weiteren danke ich Dr. Volker Tympel für die gute Zusammenarbeit und die professionelle und tatkräftige Hilfe in vielen Bereichen.
Der gesamten Arbeitsgruppe Tieftemperaturphysik und den Kollegen vom CERN Cryolab danke ich für das überaus freundschaftliche Arbeitsklima und die vielfältigen gemeinsamen Aktivitäten.
Ich danke meiner Familie und meinen Freunden für die Motivation und die gelegentlich notwendige Ablenkung. Der größte Dank gilt meinen Eltern. Vielen Dank für die Unterstützung sowie Euren motivierenden Beistand während meines gesamten Studiums!